frontiers | Frontiers in Cellular and Infection Microbiology

TYPE Original Research
PUBLISHED 07 November 2024
DOI 10.3389/fcimb.2024.1480076

OPEN ACCESS

EDITED BY
Sheila Nardelli,
Oswaldo Cruz Foundation, Brazil

REVIEWED BY
Melisa Saye,
Instituto de Investigaciones Medicas (IDIM, UBA-CONICET), Argentina
Estefanía Calvo Alvarez,
University of Milan, Italy

*CORRESPONDENCE
Juliane Wunderlich
juliane.wunderlich@mail.mcgill.ca

†PRESENT ADDRESS
Juliane Wunderlich,
Robert Koch Institute, Department of Infectious Disease Epidemiology, Berlin, Germany
Jan Strauss,
German Maritime Center, Hamburg, Germany

RECEIVED 13 August 2024
ACCEPTED 14 October 2024
PUBLISHED 07 November 2024

CITATION
Wunderlich J, Kotov V, Votborg-Novél L, Ntalla C, Geffken M, Peine S, Portugal S and Strauss J (2024) Iron transport pathways in the human malaria parasite *Plasmodium falciparum* revealed by RNA-sequencing. *Front. Cell. Infect. Microbiol.* 14:1480076. doi: 10.3389/fcimb.2024.1480076

Iron transport pathways in the human malaria parasite *Plasmodium falciparum* revealed by RNA-sequencing

Juliane Wunderlich[1,2*†], Vadim Kotov[2], Lasse Votborg-Novél[1], Christina Ntalla[1], Maria Geffken[3], Sven Peine[3], Silvia Portugal[1] and Jan Strauss[2†]

[1]Malaria Parasite Biology Group, Max Planck Institute for Infection Biology (MPIIB), Berlin, Germany, [2]Membrane Protein Structural Biology Group, Center for Structural Systems Biology (CSSB), Hamburg, Germany, [3]Institute of Transfusion Medicine, University Medical Center Hamburg-Eppendorf (UKE), Hamburg, Germany

Host iron deficiency is protective against severe malaria as the human malaria parasite *Plasmodium falciparum* depends on bioavailable iron from its host to proliferate. The essential pathways of iron acquisition, storage, export, and detoxification in the parasite differ from those in humans, as orthologs of the mammalian transferrin receptor, ferritin, or ferroportin, and a functional heme oxygenase are absent in *P. falciparum*. Thus, the proteins involved in these processes may be excellent targets for therapeutic development, yet remain largely unknown. Here, we show that parasites cultured in erythrocytes from an iron-deficient donor displayed significantly reduced growth rates compared to those grown in red blood cells from healthy controls. Sequencing of parasite RNA revealed diminished expression of genes involved in overall metabolism, hemoglobin digestion, and metabolite transport under low-iron versus control conditions. Supplementation with hepcidin, a specific ferroportin inhibitor, resulted in increased labile iron levels in erythrocytes, enhanced parasite replication, and transcriptional upregulation of genes responsible for merozoite motility and host cell invasion. Through endogenous GFP tagging of differentially expressed putative transporter genes followed by confocal live-cell imaging, proliferation assays with knockout and knockdown lines, and protein structure predictions, we identified six proteins that are likely required for ferrous iron transport in *P. falciparum*. Of these, we localized *Pf*VIT and *Pf*ZIPCO to cytoplasmic vesicles, *Pf*MRS3 to the mitochondrion, and the novel putative iron transporter *Pf*E140 to the plasma membrane for the first time in *P. falciparum*. *Pf*NRAMP/*Pf*DMT1 and *Pf*CRT were previously reported to efflux Fe^{2+} from the digestive vacuole. Our data support a new model for parasite iron homeostasis, in which *Pf*E140 is involved in iron uptake across the plasma membrane, *Pf*MRS3 ensures non-redundant Fe^{2+} supply to the mitochondrion

as the main site of iron utilization, *Pf*VIT transports excess iron into cytoplasmic vesicles, and *Pf*ZIPCO exports Fe^{2+} from these organelles in case of iron scarcity. These results provide new insights into the parasite's response to differential iron availability in its environment and into the mechanisms of iron transport in *P. falciparum* as promising candidate targets for future antimalarial drugs.

KEYWORDS

***Plasmodium falciparum*, malaria, drug target, iron deficiency, transporters, nutrient uptake, gene expression, AlphaFold**

1 Introduction

Iron is an essential micronutrient for all living organisms and has been associated with virulence of many pathogens. Iron abundance increases the replication of human immunodeficiency virus (HIV) (Drakesmith and Prentice, 2008) and *Mycobacterium tuberculosis* (Zhang et al., 2020), and promotes biofilm formation in *Pseudomonas aeruginosa* (Kang and Kirienko, 2018). A "fight for iron" has been described between bacteria and the human host in the gastrointestinal tract (Sousa Gerós et al., 2020), where the metal skews the composition of the gut microbiome by facilitating the growth of enteropathogenic *Escherichia coli* and *Salmonella* (Paganini and Zimmermann, 2017). Similarly, cancer cells require more iron compared to healthy cells (Brown et al., 2020) and higher ferritin levels in individuals diagnosed with COVID-19 were associated with increased disease severity and lethality (Taneri et al., 2020).

Host iron deficiency is known to be protective against severe malaria (Nyakeriga et al., 2004; Gwamaka et al., 2012; Clark et al., 2014; Brabin et al., 2020) and iron chelators have cytocidal effects on the human malaria parasite *Plasmodium falciparum* (Thipubon et al., 2015). This obligate intracellular parasite depends on bioavailable iron for its proliferation and relies entirely on the host to meet its nutrient requirements (Scholl et al., 2005). Furthermore, *P. falciparum* senses environmental fluctuations (Brancucci et al., 2017; Mancio-Silva et al., 2017; Chou et al., 2018) and modulates its virulence in response (Mancio-Silva et al., 2017). While iron is crucial for DNA replication and repair, mitochondrial electron transport, and redox regulation, it becomes toxic when in excess, as it is a source of damaging reactive oxygen species (Sigala and Goldberg, 2014). Importantly for therapeutic development, the mechanisms of iron acquisition, storage, detoxification, and export in the parasite are different from those in humans, as orthologs of the mammalian transferrin receptor, ferritin, or ferroportin, and a functional heme oxygenase are absent in *Plasmodium* (Mach and Sutak, 2020).

While human blood plasma contains between 10 and 30 μM total iron and an erythrocyte carries approximately 20 mM Fe (Egan et al., 2002), only 3 μM labile iron is present in the cytosol of uninfected red blood cells, and 1.6 μM in *P. falciparum*-infected ones (Loyevsky et al., 1999). An estimated total iron concentration of 500 mM (Becker et al., 2004) is reached within the parasite's digestive vacuole (DV), where iron-containing hemoglobin (Hb) is digested and the released heme is detoxified by biocrystallization into hemozoin (Wunderlich et al., 2012). However, *P. falciparum* cannot access this iron source and is thought to acquire bioavailable Fe^{2+} from the host cell (Kloehn et al., 2020). Over-elevated ferrous iron levels likely compromise the integrity of the DV membrane and cytosolic iron also needs to be regulated to prevent oxidative stress (Mach and Sutak, 2020). Iron detoxification in the parasite can be achieved by translocating the metal ion into dynamic intracellular Fe^{2+} stores, which may include acidocalcisomes – cytoplasmic vesicles that contain high concentrations of phosphate, calcium, iron, and zinc (Huang et al., 2014). In contrast to *Trypanosoma brucei* (Huang et al., 2014), no transport proteins have yet been experimentally shown to localize to the acidocalcisome membrane in *P. falciparum* (Magowan et al., 1997; Ruiz et al., 2004). Like the DV, these organelles are thought to be acidified by the plant-like V-ATPase and their low internal pH may fuel secondary active transport processes (Wunderlich et al., 2012; de Oliveira et al., 2021).

P. falciparum encodes approximately 200 transmembrane or membrane-associated transport proteins (channels, pores, carriers, and pumps), many of which are essential for parasite growth and lack human homologs (Wunderlich, 2022). For instance, the vacuolar iron transporter *Pf*VIT (PF3D7_1223700), an ortholog of *Arabidopsis thaliana* VIT1 (expect value (E) = 5 x 10^{-29}, 30.5% identity, 87% coverage, as determined by position-specific iterated BLAST (Altschul et al., 1997)), is a Fe^{2+}/H^{+} exchanger that plays a role in iron detoxification (Slavic et al., 2016; Labarbuta et al., 2017; Sharma et al., 2021). While its orthologs were localized to the endoplasmic reticulum in *Plasmodium berghei* (Slavic et al., 2016) and to the vacuolar compartment in *Toxoplasma gondii* (Aghabi et al., 2023), the subcellular localization in *P. falciparum* had not been investigated experimentally prior to this study. Similarly, the Zrt-, Irt-like protein domain-containing protein (ZIPCO) was suggested to import Fe^{2+} and Zn^{2+} into the cytosol and localized to the parasite plasma membrane (PPM) in *P. berghei* sporozoites in indirect immunofluorescence assays (Sahu et al., 2014), but *Pf*ZIPCO (ZIP domain-containing protein, PF3D7_1022300) had not been studied yet. The chloroquine resistance transporter *Pf*CRT (PF3D7_0709000) and the natural resistance-associated macrophage protein *Pf*NRAMP (PF3D7_0523800, also called *Pf*DMT1 for divalent metal transporter 1, although this

abbreviation is already in use for the drug/metabolite transporter 1) have been detected at the digestive vacuolar (DV) membrane (Waller et al., 2003; Wichers et al., 2022). Both proteins were proposed to export Fe^{2+} into the cytosol in symport with protons on the basis of transport assays using *Xenopus* oocytes (Bakouh et al., 2017) and proliferation assays with a conditional knockdown line under different iron conditions (Loveridge and Sigala, 2024), respectively.

In *Saccharomyces cerevisiae*, a model organism for eukaryotic iron homeostasis, the mitochondrial carrier protein MRS3 (mitochondrial RNA-splicing protein 3) was shown to ensure Fe^{2+} supply to the mitochondrion (Mühlenhoff et al., 2003; Froschauer et al., 2009; Brazzolotto et al., 2014) and its ortholog *Tg*MIT (mitochondrial iron transporter) was detected at the same organelle in *T. gondii* (Aghabi et al., 2023). The mitochondrion of *P. falciparum* is also the focal point for cellular iron metabolism and contains iron-dependent proteins implicated in the biosynthesis of heme and iron-sulfur clusters, redox reactions, and electron transport (Mach and Sutak, 2020). Because of sequence similarity (35.1% identity with the yeast ortholog, $E = 3 \times 10^{-14}$, 26% coverage), it was proposed that *Pf*MRS3 (also known as mitoferrin (*Pf*MFRN), PF3D7_0905200) mediates Fe^{2+} import into the mitochondrion in *P. falciparum* (Mather et al., 2007). However, no experimental evidence was collected and it is known that not only the localization but also the structure and function of homologous proteins can vary in related apicomplexan parasites (Mather et al., 2007; Sloan et al., 2021).

Despite the importance of iron for *P. falciparum* virulence, the fundamental understanding of the molecular mechanisms of iron sensing, acquisition, utilization, and regulation in the parasite remains limited. The goal of this exploratory study was to dissect how the parasite responds to differences in iron availability in its environment and to identify putative iron transporters as potential new antimalarial drug targets. We investigated growth and gene expression of the laboratory *P. falciparum* strain 3D7 under control (iron-replete), high-iron and low-iron conditions, and in the presence of the iron-regulatory peptide hormone hepcidin. In the human body, hepcidin is produced to reduce the concentration of serum iron when it rises above a certain threshold. The hormone binds specifically to ferroportin on the surface of many cell types including erythrocytes (Zhang et al., 2018) and can sterically inhibit the transporter's iron export activity, thereby increasing intracellular and decreasing serum iron levels (Aschemeyer et al., 2018; Billesbølle et al., 2020). Here, whole-transcriptome sequencing was used to identify putative iron transport proteins on the basis of differential gene expression patterns between high vs. low-iron conditions. We then characterized these proteins by analyzing their subcellular localization in live parasites, their predicted 3D structures, and the growth rates of the respective knockout or knockdown parasite lines under various iron conditions.

2 Materials and methods

2.1 *P. falciparum* culture and proliferation assays

The *P. falciparum* strain 3D7 was cultured according to modified standard procedures (Trager and Jensen, 1976) at 5% hematocrit using human 0 Rh+ erythrocytes from the University Medical Center Hamburg-Eppendorf (UKE), Germany, at 1% O_2, 5% CO_2 and 94% N_2. RPMI 1640 medium was supplemented with 0.5% (w/v) AlbuMAX II, 20 µg/mL gentamicin and 100 µM hypoxanthine (Thermo Fisher Scientific). Mature schizonts were obtained by treating schizonts at 40 hours post invasion (hpi) with 1 mM compound 2 (4-[7-[(dimethylamino)methyl]-2-(4-fluorphenyl)imidazo[1,2-α]pyridine-3-yl]pyrimidin-2-amine, LifeArc) for 8 h. To count the number of merozoites per mature schizont, Giemsa-stained blood smears were analyzed by light microscopy. Only single-infected cells with one digestive vacuole were taken into account.

To assess parasite proliferation over six days, a previously described assay on the basis of flow cytometry was employed (Malleret et al., 2011). Parasites were synchronized to a 3-h age window by isolating late schizonts from a 60% Percoll (GE Healthcare) gradient and culturing these for 3 h with fresh erythrocytes (Rivadeneira et al., 1983), followed by controlled elimination of advanced parasite stages using 5% (w/v) D-sorbitol (Carl Roth) for 10 min at 37°C (Lambros and Vanderberg, 1979). The growth assay was started at 0.1% parasitemia using the resulting ring-stage parasites at 0 – 3 hpi. The parasitemia was determined at the trophozoite stage every two days by flow cytometry and culture media with the respective supplements were exchanged daily.

2.2 Flow cytometry

To determine parasitemia, 20 µL of resuspended parasite culture was added to 80 µL culture medium and stained with 5 µg/mL SYBR Green I (Thermo Fisher Scientific) and 4.5 µg/mL dihydroethidium (DHE, Sigma-Aldrich) in the dark for 20 min at room temperature. Stained cells were washed with PBS three times and analyzed with an ACEA NovoCyte flow cytometer and NovoExpress Software (version 1.6.1, Agilent). Forward and side scatter gating was used to identify erythrocytes and SYBR Green I fluorescence intensity to determine the number of parasitized cells per 100,000 events recorded for each replicate. For Phen Green SK measurements, uninfected erythrocytes were washed with PBS and incubated with 10 µM Phen Green SK in PBS at 37°C for 60 min. DHE at 4.5 µg/mL was added during the last 20 min of incubation. After three washes with PBS, the cells were analyzed as described above.

2.3 Sample collection for RNA extraction and RNA sequencing

Parasites were synchronized to a three-hour window after invasion of erythrocytes from the respective donor as described above. Samples for RNA-sequencing were prepared in triplicate for each condition and time point, i.e., three separate parasite cultures each were grown in parallel for a total of at least two weeks. During the second IDC, two 10-mL dishes each were harvested for parasites at the ring stage (6 – 9 hpi) and one 10-mL dish each for

trophozoites (26 – 29 hpi). Samples were collected by centrifuging the culture for 5 min at 800 g and 37°C and dissolving the erythrocyte pellet using 5 mL TRIzol (ThermoFisher Scientific) prewarmed to 37°C, followed by immediate transfer to -80°C for storage. The parasitemia was 0.3% at the start of the experiments with high, control and low-iron donor blood and 2 – 3% at the time of harvest. Parasite cultures treated with 0.7 µM hepcidin (Bachem) had a starting parasitemia of 0.6% and untreated cultures 1% to reach a parasitemia of 4 – 5% during the second cycle. For each experiment, the parasitemia was kept consistent at the point of harvest as high parasite densities can affect transcription (Chou et al., 2018).

For RNA extraction, the samples frozen in TRIzol were thawed, mixed thoroughly with 0.1 volume cold chloroform, and incubated at room temperature for 3 min. Following centrifugation at 20,000 g and 4°C for 30 min, the supernatants were transferred to fresh vials and combined with 70% ethanol of equal volume. RNA was purified using the RNeasy MinElute Kit (Qiagen) by on-column DNase I digest for 30 min and elution with 14 µL water. The GLOBINclear Human Kit (ThermoFisher Scientific) was then employed to deplete human globin mRNA in all samples. The Qubit RNA HS Assay Kit and Qubit 3.0 fluorometer (ThermoFisher Scientific) were used for RNA quantification. Upon arrival at the EMBL Genomics Core Facility (GeneCore Heidelberg, Germany), the RNA quality of each sample was evaluated using the RNA 6000 Nano kit and Bioanalyzer 2100 (Agilent). The median RNA integrity number (RIN) of all samples was 7.30 (IQR: 6.85 – 8.15, Supplementary Figure S1). Individually barcoded strand-specific libraries for mRNA sequencing were prepared from total RNA samples of high quality (approximately 150 ng per sample) using the NEBNext® RNA Ultra II Directional RNA Library Prep Kit (New England Biolabs) for 12 PCR cycles on the liquid handler Biomek i7 (Beckman Coulter) at GeneCore. Libraries that passed quality control were pooled in equimolar amounts, and a 2 pM solution of this pool was sequenced unidirectionally on a NextSeq® 500 System (Illumina) at GeneCore, resulting in about 500 million reads of 85 bases each.

2.4 RNA-sequencing read mapping and data analysis

Following successful initial quality control of the RNA-sequencing reads with FastQC version 0.11.8 (Andrews, 2010), sequencing adapters were trimmed using Cutadapt version 2.10 (Martin, 2011). A genome index was generated using the FASTA sequence file of the *P. falciparum* 3D7 genome release 46 (PlasmoDB-46_Pfalciparum3D7_Genome.fasta) and the GFF3 annotation file (PlasmoDB-46_Pfalciparum3D7.gff), both obtained from PlasmoDB (Aurrecoechea et al., 2009), with STAR version 2.7.5c (Dobin et al., 2013). The same R package was used to align reads to the genome with a maximum of three allowed mismatches (–outFilterMismatchNmax 3). To consolidate the results obtained with FastQC and STAR alignments, a single report file was created using MultiQC version 1.9 (Ewels et al., 2016).

The mapped reads were then summarized in Sequence Alignment/Map (SAM) format using featureCounts (Liao et al., 2014) from the R package Rsubread version 2.2.1 (Liao et al., 2013). For counting mapped reads per gene using featureCounts, fragments with a minimum length of 50 bases were considered (minFragLength = 50). Therefore, gene IDs and lengths of transcripts were extracted from PlasmoDB-46_Pfalciparum3D7_AnnotatedTranscripts.fasta with SAMtools faidx version 1.10.2 (Li et al., 2009). The R package edgeR 3.30.3 (Robinson et al., 2010) was used to compute RPKM values (reads per kilobase per million mapped reads) and for differential gene expression analysis. Gene annotations were retrieved from PlasmoDB (Aurrecoechea et al., 2009) and PhenoPlasm (Sanderson and Rayner, 2017). The results of these analyses were visualized with volcano plots using the R package Enhanced Volcano version 1.15.0 (Blighe et al., 2022). The raw and processed data (FASTA files, RPKM values and results of the differential gene expression analysis) can be accessed at https://www.ebi.ac.uk/biostudies/studies/E-MTAB-13411.

The highly polymorphic *var*, *stevor*, and *rifin* gene families were excluded from downstream analyses because of their great sequence diversity between parasites of the same strain during mitotic growth (Bozdech et al., 2003; Kidgell et al., 2006). Genes that were significantly regulated (defined as $P < 0.05$ according to the exact test for the negative binomial distribution with Benjamini-Hochberg correction (Benjamini and Hochberg, 1995) and an absolute value of $\log_2$ FC ≥ 0.2) were subjected to functional enrichment analysis with g:Profiler (https://biit.cs.ut.ee/gprofiler/gost (Raudvere et al., 2019), accessed on August 17, 2022). The resulting GO, KEGG and REAC terms were summarized using REVIGO (http://revigo.irb.hr/) with the similarity value set to 0.5 (Supek et al., 2011) and visualized as in Thomson-Luque et al (Thomson-Luque et al., 2021) using the scientific color map "roma" (Crameri et al., 2020). To estimate parasite age, an algorithm developed by Avi Feller and Jacob Lemieux (Lemieux et al., 2009) was adapted to use expression data from Broadbent et al (Broadbent et al., 2015) with the time points 6, 14, 20, 24, 28, 32, 36, 40, 44, and 48 hpi as reference. The code and data used were deposited to Zenodo with the record ID 7996302 (https://zenodo.org/record/7996302).

2.5 Cloning of DNA constructs

For generating the GFP reporter lines, a homologous region of approximately 800 base pairs (bp) at the 3' end of the respective gene was amplified without the stop codon from 3D7 gDNA using Phusion high fidelity DNA polymerase (New England Biolabs). A homology region of about 400 bp at the 5' end of the respective gene was used for targeted gene disruption. The fragments were then inserted into pSLI-GFP (Birnbaum et al., 2017) using Not*I* and Avr*II* restriction sites. For *glmS* constructs, pSLI-GFP-*glmS* (Burda et al., 2020) was used as a vector instead. All oligonucleotides and plasmids used in this study are listed in Supplementary Table S3.

2.6 Transfection of *P. falciparum*

As described previously (Moon et al., 2013), parasites at the late schizont stage were purified using 60% Percoll (Rivadeneira et al.,

1983) and electroporated with 50 µg DNA of the respective plasmid in a 0.2-cm gap cuvette (Bio-Rad Laboratories) using Amaxa Nucleofector 2b (Lonza). Either 4 nM WR99210 (Jacobus Pharmaceuticals) or 2 µg/mL blasticidin S (Life Technologies) was used for selecting transfectants. For the selection of parasites that were genomically modified using the SLI system (Birnbaum et al., 2017), 400 µg/mL G418 (ThermoFisher Scientific) was added to the culture medium once the parasitemia reached 5%. After the selection of modified parasites, genomic DNA was isolated with the QIAamp DNA Mini Kit (Qiagen) and diagnostic tests for correct integration into the genome were performed as specified earlier (Birnbaum et al., 2017).

2.7 Confocal live-cell microscopy

Erythrocytes infected with parasites at different stages at 3 – 6% parasitemia were incubated in culture medium with 20 nM MitoTracker Red, 200 nM ER Tracker Red or 100 nM LysoTracker Deep Red (Invitrogen, if applicable) at 37°C for 20 min. Then, 200 nM Hoechst-33342 (Invitrogen) was added for 10 min prior to washing the cells with Ringer's solution (122.5 mM NaCl, 5.4 mM KCl, 1.2 mM $CaCl_2$, 0.8 mM $MgCl_2$, 11 mM D-glucose, 25 mM HEPES, 1 mM NaH_2PO_4, pH 7.4) prewarmed to 37°C and seeding on a chambered No. 1.5 polymer cover slip (Ibidi). After 5 min, unbound erythrocytes were removed by washing with Ringer's solution and the sample was placed into an incubation chamber that maintained the microscope work area including the objective at 37°C. Images and videos were acquired using an SP8 confocal microscope system with a 63x oil-corrected lens (C-Apochromat, numerical aperture = 1.4) and Lightning deconvolution software (Leica), and processed using ImageJ version 2.9.0/1.53t (Schindelin et al., 2012). If fluorescence intensities were to be quantified, no averaging or deconvolution software was applied.

2.8 Conditional knockdown mediated by *glmS* ribozyme

For *glmS*-based knockdown induction (Prommana et al., 2013), highly synchronous parasites at the early ring stage were cultured with or without supplementation with 2.5 mM glucosamine (GlcN, Sigma-Aldrich). The knockdown was quantified by confocal live-cell microscopy using schizonts 36 h post GlcN treatment initiation. Images of parasites of similar size were acquired with the same settings and background-corrected fluorescence intensities (integrated density) as well as the size of the region of interest were determined using ImageJ version 2.9.0/1.53t (Schindelin et al., 2012), and the data visualized using Graph Pad Prism version 9.4.1.

2.9 Protein structure prediction

Structure predictions for monomeric proteins were obtained from AlphaFold Protein Structure Database version 3 (Jumper et al., 2021; Varadi et al., 2022) and homodimeric proteins were predicted using AlphaFold2-multimer version 2.2.2, database version 2.2.0 (Evans et al., 2022) deployed at the EMBL Hamburg computer cluster. Molecular visualization was performed with UCSF ChimeraX version 1.3 (Goddard et al., 2018). UCSF Chimera MatchMaker and Match → Align tools with default settings were used for structural comparison of the predicted structures of *P. falciparum* proteins with putative orthologs and sequence alignments were generated using the Match → Align tool (Meng et al., 2006). The DeepFRI server (https://beta.deepfri.flatironinstitute.org) was used to identify possible functional residues with the DeepFRI graph convolutional network (Gligorijević et al., 2021).

3 Results

3.1 Elevated erythrocyte labile iron levels promote *P. falciparum* proliferation *in vitro*

To investigate whether labile iron levels in the erythrocyte correlate with parasite replication rates, we established different iron conditions *in vitro*. The first approach was to culture *P. falciparum* 3D7 parasites in 0 Rh+ erythrocytes from voluntary blood donations by Caucasians aged 18 to 21 at the University Medical Center Hamburg-Eppendorf in Germany. Therefore, samples from a person with an elevated ferritin level (greater than 200 µg/L (Marfil-Rivera, 2015), in this case 231 µg/L ferritin, 18.2 g/dL Hb, 51.5% hematocrit), an iron-deficient individual (serum ferritin < 12 ng/ml (Knovich et al., 2009), here: 3 µg/L ferritin, 11.4 g/dL Hb, 36.3% hematocrit) and a healthy donor (21 µg/L ferritin, 15.0 g/dL Hb, 42.3% hematocrit) were used. Secondly, infection of red blood cells from other healthy individuals with or without the addition of 0.7 µM hepcidin to the culture medium was compared. This concentration was chosen as it had the strongest effect on parasite proliferation in preliminary experiments, and is expected to increase intracellular Fe^{2+} as it is twice as high as the hepcidin level needed to reduce ^{55}Fe export from preloaded mature erythrocytes by 30% within one hour of incubation (Zhang et al., 2018).

Relative labile iron levels in uninfected erythrocytes were estimated by determining the mean fluorescence intensity (MFI) of the iron-sensitive dye Phen Green SK in 100,000 cells per replicate using flow cytometry. As binding of ferrous iron to the metal-binding moiety causes fluorescence quenching of the fluorophore, a reduction in fluorescence intensity indicates higher labile iron levels (Petrat et al., 1999). In erythrocytes from the iron-deficient donor, the Phen Green SK MFI was 43% higher relative to control, confirming reduced labile iron levels (Figure 1A). The parasite replication rate after one intraerythrocytic developmental cycle (IDC) decreased by 16% (Figure 1B), the DNA content of late schizonts by 19% (Figure 1C) and the number of merozoites counted per late schizont by 14% (Figure 1D). In contrast, labile iron levels of erythrocytes from the donor with higher iron status were only slightly increased (without statistical support, two-tailed unpaired *t* tests with Welch's correction for unequal variances and adjusted with the Holm-Šídák method for multiple comparisons, $P = 0.25$) relative to blood with normal iron level (healthy control) – as were the parasite proliferation rate, the DNA

content and the merozoite number of mature schizonts (Figure 1). To further increase intracellular labile iron levels, we incubated parasites with 0.7 µM hepcidin during one IDC, resulting in 11% reduced Phen Green SK MFI compared to control (Figure 1A). Under these conditions, the parasite growth rate increased by 57% (Figure 1B), the DNA content per schizont by 16% (Figure 1C), and the number of merozoites produced per schizont by 15% (Figure 1D).

Taken together, these data show that parasites grown in erythrocytes from an iron-deficient donor displayed significantly reduced growth rates compared to healthy control. Our *in vitro* results also demonstrate that hepcidin treatment of control erythrocytes elevated intracellular Fe^{2+} concentrations and promoted parasite proliferation.

3.2 RNA-sequencing reveals differential expression of iron transporter genes

To identify iron-regulated mechanisms and putative iron transporters in *P. falciparum*, we carried out whole-transcriptome profiling using bulk RNA-sequencing (Figure 2). *P. falciparum* 3D7 parasites were cultured either using erythrocytes from a donor with higher, control (healthy) or low iron status (experiment 1); or with red blood cells from another healthy donor in the presence or absence of 0.7 µM hepcidin (experiment 2). Samples from three biological replicates per condition were harvested at the ring and trophozoite stage (6 – 9 hpi and 26 – 29 hpi) during the second IDC under the conditions specified.

To exclude the possibility that differences in mRNA abundance were a consequence of divergent progression through the IDC under different nutritional conditions, we assessed the average developmental age of the parasites in each sample on the basis of a statistical maximum likelihood estimation (MLE) method of transcriptional patterns according to Lemieux et al. (Lemieux et al., 2009). The general transcriptional patterns of parasites were highly similar at individual time points and consistent across different experimental treatments, corresponding to those of a 3D7 reference strain (Broadbent et al., 2015) at approximately 10 hpi and 35 hpi (Figure 2A). This indicates that differences in mRNA abundance of parasites were not caused by divergent progression through the IDC but by direct effects of the experimental treatments. As the 3D7 strain we used for the experiments had a

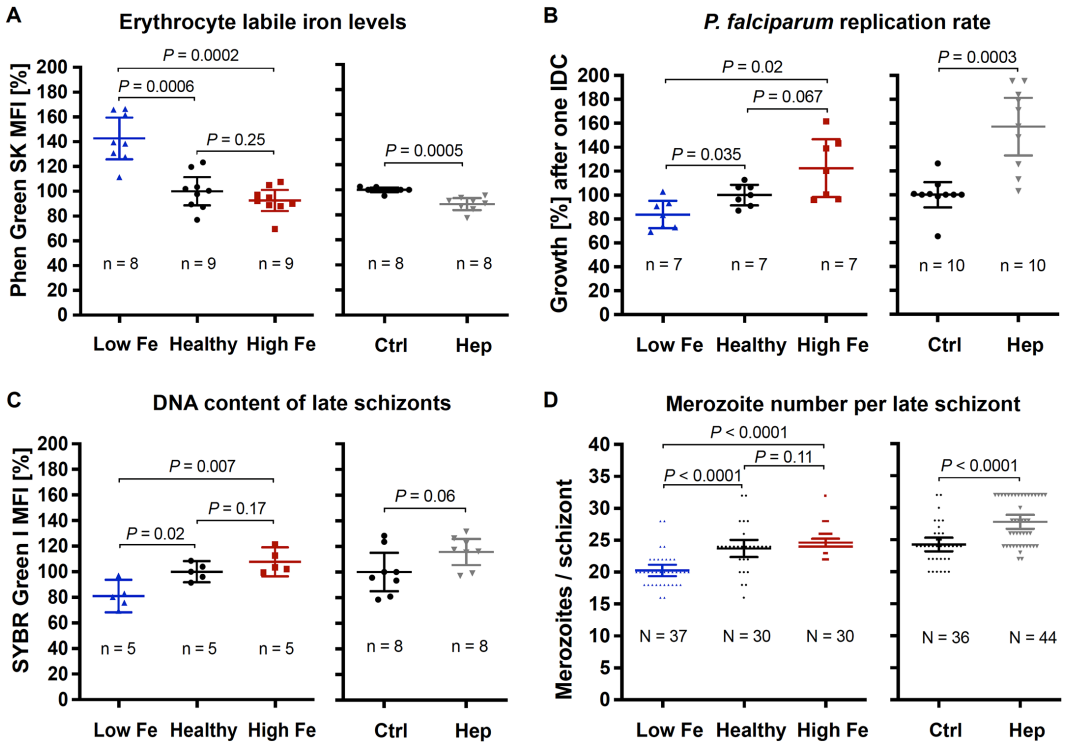

FIGURE 1
Effects of the iron status of the blood donor and of hepcidin on **(A)** erythrocyte labile iron levels, **(B)** *P. falciparum* 3D7 growth rates, **(C)** DNA content per mature schizont, and **(D)** the number of merozoites per mature schizont. The relative labile iron level and DNA content per cell were assessed in the presence or absence of 0.7 µM hepcidin (Hep) by measuring the mean fluorescence intensity (MFI) of Phen Green SK or SYBR Green I compared to control (Ctrl, untreated, normal hemoglobin level) using flow cytometry. Therefore, 100,000 cells were analyzed per replicate. Parasite growth rates refer to the fold change in parasitemia after one intraerythrocytic developmental cycle *in vitro* relative to control as determined by flow cytometry with SYBR Green I (Malleret et al., 2011). Mature schizonts were obtained by treating schizonts at 40 hpi with 1 mM compound 2 (4-[7-[(dimethylamino)methyl]-2-(4-fluorphenyl)imidazo[1,2-α]pyridine-3-yl]pyrimidin-2-amine) for 8 h. To count the number of merozoites, Giemsa-stained blood smears were analyzed microscopically and only single-infected cells with one digestive vacuole were considered. Means and 95% confidence intervals (indicated by error bars) are shown. Statistical significance was calculated with two-tailed unpaired *t* tests with Welch's correction for unequal variances and adjusted with the Holm-Šídák method for multiple comparisons except for merozoite numbers, which were compared using Mann-Whitney test. N represents the number of parasites and n the number of independent experiments.

10.3389/fcimb.2024.1480076

A

	Experiment 1			Experiment 2	
	Low Fe	Healthy control	High Fe	Hepcidin-treated	Untreated control
MLE of parasite age [hpi] at ring stage	9.9 (97.5% CI: 9.6 – 10.3)	10.2 (97.5% CI: 9.8 – 10.7)	10.0 (97.5% CI: 9.6 – 10.5)	10.2 (97.5% CI: 9.8 – 10.7)	10.6 (97.5% CI: 10.2 – 11.0)
MLE of parasite age [hpi] at trophozoite stage	35.4 (97.5% CI: 34.8 – 35.8)	35.5 (97.5% CI: 35.0 – 36.0)	35.4 (97.5% CI: 34.8 – 36.0)	34.7 (97.5% CI: 34.0 – 35.3)	34.5 (97.5% CI: 33.8 – 35.0)

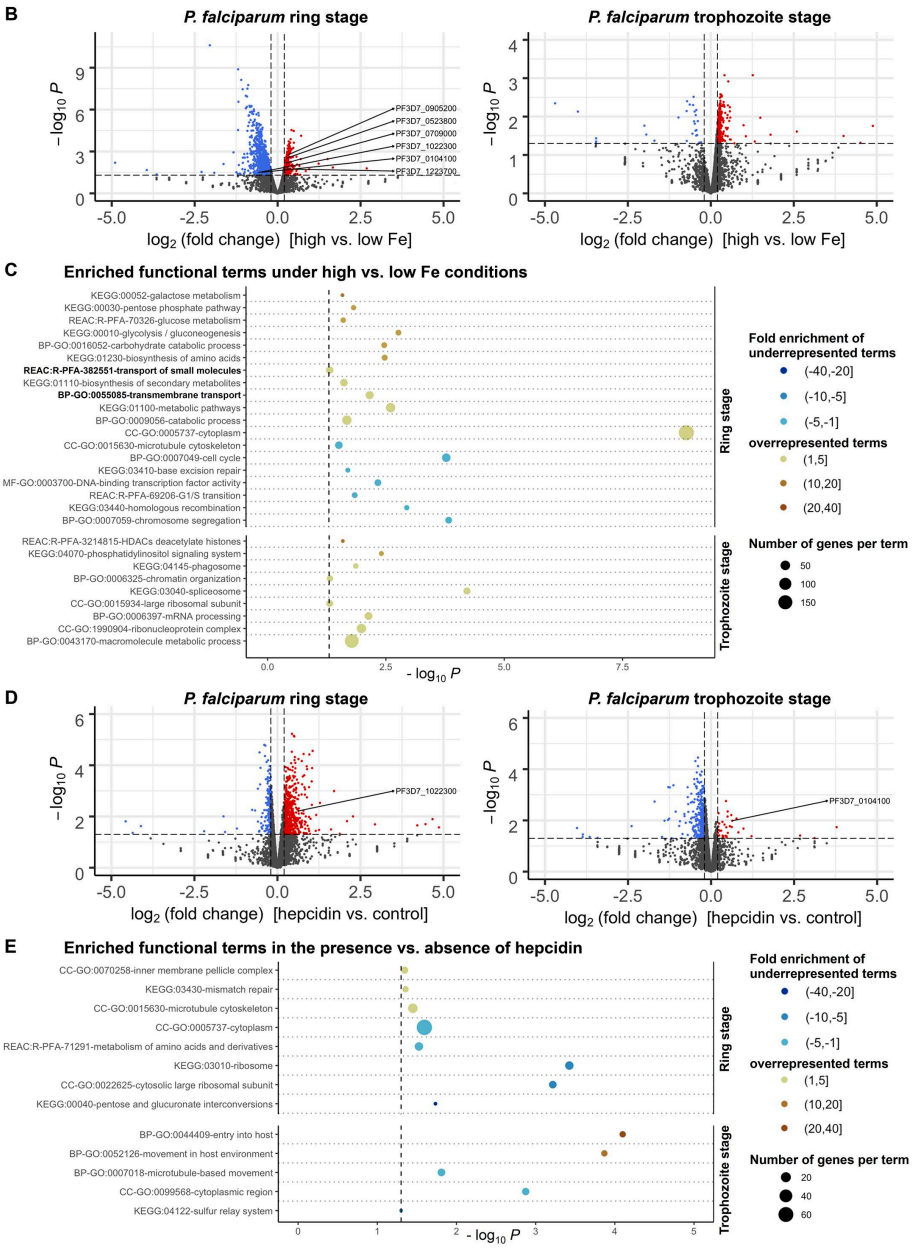

FIGURE 2
Differential expression of *P. falciparum* 3D7 genes under various iron conditions. Parasites were cultured with erythrocytes from an individual with high, medium (healthy) or low iron status (experiment 1) or with red blood cells from another healthy donor in the presence or absence of 0.7 µM hepcidin (experiment 2). Samples were harvested at the ring and trophozoite stage (6 – 9 and 26 – 29 hours post invasion, hpi) with three biological replicates per time point and condition. The maximum likelihood estimation (MLE) of the average developmental age of the parasites for each condition and time point **(A)** was calculated using an algorithm developed by Avi Feller and Jacob Lemieux (Lemieux et al., 2009). CI, confidence interval. The volcano plots **(B, D)** show transcriptional changes of all parasite genes. Red dots indicate significantly ($P < 0.05$, exact test for negative binomial distribution) upregulated genes ($\log_2$ (fold change) ≥ 0.2), blue dots stand for significantly downregulated genes ($\log_2$ (fold change) ≤ -0.2), while grey dots represent genes that did not significantly differ in transcription under the conditions described ($P \geq 0.05$ and/or $-0.2 < \log_2$ (fold change) < 0.2). Differentially expressed genes encoding putative iron transporters (see Table 1) are labeled. Panels **(C, E)** show the enrichment of Gene Ontology (GO), Kyoto Encyclopedia of Genes and Genomes (KEGG) and Reactome (REAC) terms among significantly regulated genes excluding *var, stevor* and *rifin* gene families at the two time points. The functional terms were summarized using REVIGO (Supek et al., 2011) to remove redundancies, represented by circles and plotted according to the significance of their enrichment ($-\log_{10}$ (adjusted P), hypergeometric test). The size of the circle is proportional to the number of differentially regulated genes in the dataset that are associated with the respective term, while the color stands for the fold enrichment. The gray dashed line indicates the threshold of the adjusted P value ($-\log_{10}$ 0.05 = 1.3).

reduced total IDC length of 44 h instead of 48 h, possibly because of gene deletions that may have occurred during long-term culturing (Wichers et al., 2019; Stewart et al., 2020), it progresses through the cycle faster than the 3D7 reference strain (Broadbent et al., 2015). This may explain why the calculated MLEs of parasite age were higher than the actual values of 6 – 9 hpi and 26 – 29 hpi (Figure 2A).

Using a threshold of 1.5 for the fold change (FC) in gene expression (log_2 FC of 0.585 or -0.585) yielded twelve significantly upregulated and 175 downregulated genes in ring-stage parasites under high vs. low-iron conditions ($P < 0.05$, exact test for the negative binomial distribution with Benjamini-Hochberg correction (Benjamini and Hochberg, 1995)). As differences in transporter gene transcription are typically small (Küpper and Kochian, 2010; Abrahamian et al., 2016), we examined the 351 upregulated and 770 downregulated genes with a significant expression change and a minimum absolute value of the log_2 FC of 0.2 for this comparison (Figure 2B). The full RNA-sequencing datasets are available in the BioStudies repository (Sarkans et al., 2018) under accession number E-MTAB-13411 (https://www.ebi.ac.uk/biostudies/studies/E-MTAB-13411) and differential gene expression test results for individual genes are shown in Supplementary Tables S1 and S2. The highly polymorphic *var*, *stevor*, and *rifin* gene families were excluded from downstream analyses because of their significant sequence diversity between parasites of the same strain during mitotic growth (Bozdech et al., 2003; Kidgell et al., 2006). Functional Gene Ontology (GO), Kyoto Encyclopedia of Genes and Genomes (KEGG) and Reactome (REAC) term enrichment analyses of differentially expressed genes (DEGs) were performed using the g:Profiler web server (Raudvere et al., 2019).

Under high vs. low-iron conditions at the ring stage (6 – 9 hpi), the GO term for biological process GO:0055085 "transmembrane transport" was 2.8-fold enriched ($P = 0.007$, hypergeometric test) among significantly upregulated parasite genes (Figure 2C). Using the recently updated *P. falciparum* transporter list (Wunderlich, 2022), all genes with differential expression levels at the ring stage were then screened for transport proteins and all of the five genes previously proposed as iron transporters in *Plasmodium* (VIT, ZIPCO, NRAMP/DMT1, CRT, MRS3/MFRN (Mach and Sutak, 2020; Sloan et al., 2021)) were found differentially expressed (Table 1). The putative transporter *Pf*E140 (Wunderlich, 2022), which is predicted to be essential (Zhang et al., 2018), may also be involved in iron transport, as it was differentially expressed under low-iron vs. control conditions at the ring stage (Table 1) as well as in the presence vs. absence of hepcidin in trophozoites (Figure 2D). Other significantly enriched functional terms at the ring stage under high-iron conditions were GO:0009056 "catabolic process", GO:0020020 "food vacuole", KEGG:01100 "metabolic pathways", and GO:0005737 "cytoplasm" (Figure 2C). Among downregulated genes under high vs. low-iron conditions at the ring stage, KEGG:03440 "homologous recombination", KEGG:03410 "base excision repair", GO:0007049 "cell cycle", and GO:0015630 "microtubule cytoskeleton" were enriched (Figure 2C). At the more metabolically active trophozoite stage (26 – 29 hpi), processes related to mRNA splicing and protein production were overrepresented in upregulated genes, as indicated by the 2.9-fold enrichment ($P = 0.00006$) of the KEGG:03040 pathway "spliceosome" and the 2.5-fold enrichment ($P < 0.05$) of the GO:0015934 term "large ribosomal subunit" (Figure 2C).

In contrast, hepcidin treatment resulted in reduced metabolism compared to control conditions, as KEGG:00040 "pentose and glucuronate interconversions", REAC:R-PFA-71291 "metabolism of amino acids and derivatives", GO:0005737 "cytoplasm", and GO:0015934 "large ribosomal subunit" were significantly enriched in downregulated genes during the parasite ring stage at 6 – 9 hpi (Figure 2E). Among significantly upregulated genes in the presence vs. absence of hepcidin, the terms GO:0070258 "inner membrane pellicle complex" ($P < 0.05$), KEGG:03430 "mismatch repair" ($P = 0.04$), and GO:0015630 "microtubule cytoskeleton" ($P = 0.04$) were enriched at the ring stage. GO:0044409 "entry into host" ($P = 0.00008$) and GO:0052126 "movement in host environment" ($P = 0.0001$) were overrepresented at the trophozoite stage (Figure 2E), possibly linked to the observed increase in parasite proliferation (Figure 1B).

Our RNA-sequencing data also revealed the differential expression of genes involved in epigenetic, transcriptional, translational, and post-translational regulation. Under high vs. low-iron conditions, histone deacetylation and chromatin organization processes as well as GO:1990904 "ribonucleoprotein complex" were significantly enriched in upregulated genes at the trophozoite stage, and GO:000370 "DNA binding transcription factor activity" in downregulated genes at the ring stage (Figure 2C). Furthermore, the known iron-regulatory protein *Pf*IRP or aconitate hydratase (Loyevsky et al., 2001; Hodges et al., 2005) was upregulated during the ring stage under high vs. low-iron conditions (log_2 FC = 0.49, $P = 0.00003$) and downregulated in the presence of hepcidin (log_2 FC = -0.27, $P = 0.01$) as compared to control. Many protein kinases involved in post-translational modifications and endocytosis were also upregulated at 26 – 29 hpi at high vs. low iron levels, as indicated by the enriched terms GO:0043170 "macromolecule metabolic process" and KEGG:04070 "phosphatidylinositol signaling system" (Figure 2C).

3.3 Localization of *Pf*MRS3, *Pf*VIT, *Pf*ZIPCO, and *Pf*E140 in *P. falciparum*

On the basis of transcriptomic profiles and the *P. falciparum* transporter list (Wunderlich, 2022), six proteins with a potential role in iron transport were identified (Tables 1, 2). The subcellular localization of the four proteins that had not yet been localized in *P. falciparum* (*Pf*MRS3, *Pf*VIT, *Pf*ZIPCO, and *Pf*E140) was then examined by endogenous tagging with GFP and confocal imaging of live parasites under physiological control conditions. At least two cell lines were generated per transporter candidate with consistent results and representative example images are shown in Figure 3. Diagnostic PCRs confirmed the fusion of *gfp* to the respective gene of interest and the absence of parental DNA at the original locus (Supplementary Figure S2). Only the *Pf*MRS3 reporter cell line still contained wild-type DNA of the parental parasites even after prolonged WR99210/G418 selection and limiting dilution cloning

10.3389/fcimb.2024.1480076

TABLE 1 *P. falciparum* transport proteins with differential gene expression under various iron conditions.

Gene product and ID	Log_2 (fold change) high vs. low Fe	Log_2 (fold change) low Fe vs. control	Log_2(fold change) hepcidin vs. control	Known or putative function
PLP5 (PF3D7_0819200)	+ 0.49 (P = 0.0002)	n.s.	- 0.29 (P = 0.003)	Host cell permeabilization and rupture (Sassmannshausen et al., 2020)
ABCG (PF3D7_1426500)	+ 0.45 (P = 0.02)	- 0.57 (P = 0.006)	n.s.	Putative metabolite exporter at PPM (Edayé and Georges, 2015), human ortholog ABCG2 exports heme (Jonker et al., 2002)
VP1 (PF3D7_1456800)	+ 0.39 (P = 0.0006)	- 0.34 (P = 0.004)	n.s.	Active H^+ export across PPM (Ahiya et al., 2022)
TOM7 (PF3D7_0823700)	+ 0.38 (P = 0.02)	n.s.	n.s.	Protein import across outer mitochondrial membrane (Sheiner and Soldati-Favre, 2008; Schmidt et al., 2010)
HlyIII (PF3D7_1455400)	+ 0.38 (P = 0.0009)	n.s.	n.s.	Forms pore (~3.2 nm) for solutes and ions in EPM (Moonah et al., 2014)
TPT (PF3D7_0508300)	+ 0.37 (P = 0.001)	- 0.40 (P = 0.002)	n.s.	Imports phosphoenolpyruvate, dihydroxyacetone, and 3-phosphoglycerate across outer apicoplast membrane (Lim et al., 2010)
V_o c (PF3D7_0519200)	+ 0.36 (P = 0.0006)	n.s.	- 0.16 (P = 0.007)	V-ATPase subunit: active H^+ export from cytosol (Hayashi et al., 2000)
MDR1 (PF3D7_0523000)	+ 0.34 (P = 0.0009)	- 0.23 (P = 0.03)	n.s.	Active drug and solute import into DV (Friedrich et al., 2014)
NT3 (PF3D7_1469400)	+ 0.34 (P = 0.03)	n.s.	n.s.	Putative nucleoside transporter (Martin et al., 2005)
SEC61α (PF3D7_1346100)	+ 0.33 (P = 0.0006)	- 0.22 (P = 0.04)	- 0.17 (P = 0.005)	ER import of proteins destined for export (Marapana et al., 2018)
MRS3 (PF3D7_0905200)	+ 0.33 (P = 0.002)	- 0.19 (P = 0.04)	n.s.	Putative Fe^{2+} importer into mitochondrial matrix (Mühlenhoff et al., 2003)
HT1 (PF3D7_0204700)	+ 0.33 (P = 0.002)	- 0.30 (P = 0.006)	n.s.	Imports glucose and fructose across PPM (Blume et al., 2011)
ATP4 (PF3D7_1211900)	+ 0.33 (P = 0.005)	- 0.40 (P = 0.002)	n.s.	H^+ import, Na^+ export across PPM (Spillman Natalie et al., 2013)
MCT2 (PF3D7_0926400)	+ 0.32 (P = 0.005)	n.s.	n.s.	Exports organic solutes from apicoplast, imports H^+ (Boucher et al., 2018)
V_1 B (PF3D7_0406100)	+ 0.30 (P = 0.001)	- 0.25 (P = 0.008)	- 0.13 (P = 0.04)	V-ATPase subunit: active H^+ export from cytosol (Hayashi et al., 2000)
V_1 A (PF3D7_1311900)	+ 0.30 (P = 0.001)	- 0.28 (P = 0.003)	- 0.20 (P = 0.001)	V-ATPase subunit: active H^+ export from cytosol (Hayashi et al., 2000)
TIM16 (PF3D7_0513500)	+ 0.29 (P = 0.03)	n.s.	n.s.	Protein import across inner mitochondrial membrane (Schmidt et al., 2010; van Esveld et al., 2021)
VIT (PF3D7_1223700)	+ 0.29 (P = 0.02)	n.s.	n.s.	Fe^{2+} sequestration from cytosol in exchange for H^+ (Slavic et al., 2016; Labarbuta et al., 2017; Sharma et al., 2021)
ApiAT2 (PF3D7_0914700)	+ 0.28 (P = 0.006)	n.s.	n.s.	Putative amino acid transporter at PPM (Wichers et al., 2021)
NRAMP (PF3D7_0523800)	+ 0.28 (P = 0.003)	n.s.	n.s.	Symport of Mn^{2+} or Fe^{2+} with H^+ from DV into cytosol (Wunderlich et al., 2012; Wichers et al., 2022)
AMC1 (PF3D7_0108800)	+ 0.26 (P = 0.03)	n.s.	n.s.	Putative mitochondrial transporter (Gardner et al., 2002)

(Continued)

TABLE 1 Continued

Gene product and ID	Log_2 (fold change) high vs. low Fe	Log_2 (fold change) low Fe vs. control	Log_2(fold change) hepcidin vs. control	Known or putative function
CRT (PF3D7_0709000)	+ 0.26 (P = 0.007)	n.s.	n.s.	Symport of positively charged dipeptides or Fe^{2+} with H^+ from DV into cytosol (Bakouh et al., 2017)
V_1 H (PF3D7_1306600)	+ 0.26 (P = 0.01)	n.s.	n.s.	V-ATPase subunit: active H^+ export from cytosol (Hayashi et al., 2000)
AAC2 (PF3D7_1004800)	+ 0.25 (P = 0.03)	n.s.	- 0.21 (P = 0.04)	Mitochondrial ADP/ATP antiporter (van Esveld et al., 2021)
PiT (PF3D7_1340900)	+ 0.24 (P = 0.02)	- 0.21 (P = 0.04)	n.s.	Imports phosphate and Na^+ into cytosol across PPM (Martin et al., 2005)
V_o d (PF3D7_1464700)	+ 0.24 (P = 0.02)	- 0.23 (P = 0.03)	- 0.15 (P = 0.02)	V-ATPase subunit: active H^+ export from cytosol (Hayashi et al., 2000)
V_o c" (PF3D7_1354400)	+ 0.23 (P = 0.03)	n.s.	n.s.	V-ATPase subunit: active H^+ export from cytosol (Hayashi et al., 2000)
ATP10 (PF3D7_0727800)	+ 0.23 (P = 0.01)	n.s.	n.s.	Active apicoplast Mn^{2+} transporter (Martin, 2020)
SulP (PF3D7_1471200)	+ 0.23 (P = 0.02)	n.s.	n.s.	Inorganic anion antiporter at PPM (Martin et al., 2005)
ATP2 (PF3D7_1219600)	+ 0.22 (P = 0.02)	- 0.22 (P < 0.05)	- 0.14 (P = 0.03)	Putative phospholipid flippase at PPM (Martin et al., 2005)
NT1 (PF3D7_1347200)	+ 0.22 (P = 0.02)	n.s.	n.s.	Purin base import across PPM (Carter et al., 2000)
AAT1 (PF3D7_0629500)	- 0.26 (P = 0.007)	n.s.	n.s.	Putative amino acid transporter at PPM and DV (Gardner et al., 2002)
MIT1 (PF3D7_1120300)	- 0.27 (P = 0.02)	n.s.	n.s.	Putative mitochondrial magnesium/nickel/cobalt ion channel (van Esveld et al., 2021)
AAT2 (PF3D7_1208400)	- 0.29 (P = 0.009)	n.s.	n.s.	Putative amino acid transporter at PPM (Martin et al., 2005)
MDR7 (PF3D7_1209900)	- 0.34 (P = 0.04)	n.s.	n.s.	Active efflux of peptides from mitochondrion (Martin et al., 2005; Mather et al., 2007)
CuTP (PF3D7_0904900)	- 0.36 (P = 0.008)	+ 0.52 (P = 0.004)	n.s.	Active Cu^{2+} export from cytoplasmic vesicle (Martin et al., 2005; Kenthirapalan et al., 2014)
GCβ (PF3D7_1360500)	- 0.36 (P = 0.007)	n.s.	n.s.	Putative phospholipid flippase at PPM (Martin et al., 2005)
TPC (PF3D7_1368700)	- 0.37 (P = 0.01)	+ 0.33 (P = 0.02)	n.s.	Thiamine pyrophosphate import, nucleotide export from mitochondrion (Martin, 2020)
F_1 γ (PF3D7_1311300)	- 0.38 (P = 0.03)	n.s.	+ 0.32 (P = 0.03)	Subunit of mitochondrial H^+-importing ATP synthase (Gardner et al., 2002)
PF3D7_0614900	- 0.43 (P = 0.005)	+ 0.72 (P = 0.0001)	+ 0.29 (P = 0.0003)	Putative ABC transporter at PPM (Wunderlich, 2022)
MFS4 (PF3D7_1203400)	- 0.44 (P = 0.0008)	+ 0.56 (P = 0.0005)	+ 0.27 (P = 0.02)	Putative transporter (Martin et al., 2005)
F_o d (PF3D7_0311800)	- 0.46 (P = 0.004)	+ 0.34 (P = 0.02)	n.s.	Subunit of mitochondrial H^+-importing ATP synthase (Martin, 2020)
PF3D7_1004600	- 0.47 (P = 0.01)	+ 0.58 (P = 0.003)	+ 0.28 (P = 0.03)	Putative ABC transporter linked to drug resistance (Park et al., 2012)
MPC2 (PF3D7_1470400)	- 0.47 (P = 0.03)	+ 0.66 (P = 0.005)	n.s.	Subunit of mitochondrial putative pyruvate:H^+ importer (Martin, 2020)
E140 (PF3D7_0104100)	- 0.47 (P = 0.03)	+ 0.65 (P = 0.006)	n.s.	Putative transport protein at PPM (Wunderlich, 2022)

(Continued)

TABLE 1 Continued

Gene product and ID	Log_2 (fold change) high vs. low Fe	Log_2 (fold change) low Fe vs. control	Log_2(fold change) hepcidin vs. control	Known or putative function
MDR4 (PF3D7_0302600)	- 0.55 ($P = 0.001$)	+ 0.63 ($P = 0.001$)	+ 0.33 ($P = 0.02$)	Active drug export across innermost apicoplast membrane (Cowell et al., 2018; Sayers et al., 2018)
ZIPCO (PF3D7_1022300)	- 0.57 ($P = 0.03$)	+ 0.55 ($P = 0.04$)	+ 0.63 ($P = 0.006$)	Fe^{2+}/Zn^{2+} import into cytosol (Sahu et al., 2014)
F_1 δ (PF3D7_1147700)	- 0.59 ($P = 0.004$)	+ 0.63 ($P = 0.005$)	n.s.	Subunit of mitochondrial H^+-importing ATP synthase (Gardner et al., 2002)
TRP-ML (PF3D7_1313500)	- 0.59 ($P = 0.01$)	+ 0.64 ($P = 0.005$)	n.s.	Putative Ca^{2+} channel (Gupta et al., 2022)
F_1 ε (PF3D7_0715500)	- 0.67 ($P = 0.04$)	+ 0.94 ($P = 0.007$)	n.s.	Subunit of mitochondrial H^+-importing ATP synthase (Gardner et al., 2002)
MFS3 (PF3D7_0919500)	- 0.85 ($P = 0.01$)	+ 0.72 ($P = 0.01$)	n.s.	Putative sugar transporter (Gardner et al., 2002)
ATP11 (PF3D7_1468600)	n.s.	+ 1.14 ($P = 0.005$)	n.s.	Putative phospholipid flippase at PPM (Martin et al., 2005; Wunderlich, 2022)
NGT (PF3D7_0505300)	n.s.	+ 0.91 ($P = 0.00008$)	+ 0.79 ($P = 0.00004$)	UDP-N-acetylglucosamine import, UMP export from Golgi (Martin et al., 2005)
SAMC (PF3D7_1241600)	n.s.	+ 0.77 ($P = 0.03$)	+ 0.68 ($P = 0.02$)	S-adenosylmethionine import into mitochondrion (Nozawa et al., 2020)
PF3D7_0614900	n.s.	+ 0.72 ($P = 0.0001$)	+ 0.29 ($P = 0.0003$)	Putative active transporter at PPM (Wunderlich, 2022)
GPH (PF3D7_0529200)	n.s.	+ 0.70 ($P = 0.03$)	n.s.	Putative sugar:cation symporter (Martin et al., 2005)
ATP9 (PF3D7_1348800)	n.s.	+ 0.62 ($P = 0.04$)	n.s.	Active Ca^{2+} import into DV? (Martin, 2020)
CTR2 (PF3D7_1421900)	n.s.	+ 0.52 ($P = 0.004$)	n.s.	Putative apicoplast copper channel (Martin, 2020)
MDR5 (PF3D7_1339900)	n.s.	+ 0.51 ($P = 0.02$)	n.s.	Active solute export across PPM (Martin, 2020)
TIC20 (PF3D7_1144700)	n.s.	+ 0.49 ($P = 0.007$)	n.s.	Protein import across innermost apicoplast membrane (Agrawal and Striepen, 2010)
PF3D7_0924500	n.s.	+ 0.47 ($P = 0.002$)	n.s.	Putative Na^+/H^+ exchanger (Saier et al., 2016)
PPT (PF3D7_0530200)	n.s.	+ 0.46 ($P = 0.02$)	n.s.	Imports phosphoenolpyruvate, dihydroxyacetone, and 3-phosphoglycerate across inner apicoplast membrane (Lim et al., 2010)
CLAG3.1 (PF3D7_0302500)	n.s.	+ 0.45 ($P < 0.05$)	n.s.	Purine, amino acid, sugar, and vitamin import across EPM (Schureck et al., 2021)
CDF (PF3D7_0715900)	n.s.	+ 0.44 ($P = 0.02$)	n.s.	Putative Zn^{2+} importer (Sloan et al., 2021) into cytoplasmic vesicles (Wichers et al., 2022)
ATP7 (PF3D7_0319000)	n.s.	+ 0.44 ($P = 0.007$)	n.s.	Putative phospholipid flippase at PPM (Martin et al., 2005; Wunderlich, 2022)
RhopH3 (PF3D7_0905400)	n.s.	+ 0.42 ($P = 0.04$)	n.s.	Purine, amino acid, sugar, and vitamin import across EPM (Schureck et al., 2021)
AQP2 (PF3D7_0810400)	n.s.	+ 0.34 ($P = 0.02$)	- 0.19 ($P < 0.05$)	Water channel at PPM (Chitale et al., 2009)
MFS2 (PF3D7_0916000)	n.s.	+ 0.33 ($P = 0.04$)	n.s.	Putative sugar transporter (Martin et al., 2005)
TFP1 (PF3D7_0206200)	n.s.	+ 0.33 ($P = 0.02$)	n.s.	Putative metabolite transporter at PPM (Martin, 2020)
ATP6 (PF3D7_0106300)	n.s.	- 0.22 ($P = 0.03$)	n.s.	Active Ca^{2+}{sp}{/sp} import into ER for storage (Martin, 2020)

(Continued)

TABLE 1 Continued

Gene product and ID	Log_2 (fold change) high vs. low Fe	Log_2 (fold change) low Fe vs. control	Log_2(fold change) hepcidin vs. control	Known or putative function
V_1 G (PF3D7_1323200)	n.s.	- 0.23 (P = 0.04)	- 0.12 (P = 0.04)	V-ATPase subunit: active H^+ export from cytosol (Hayashi et al., 2000)
FNT (PF3D7_0316600)	n.s.	- 0.27 (P = 0.02)	- 0.16 (P = 0.004)	Lactate/formate and H^+ release from cytosol (Martin, 2020)
MFR1 (PF3D7_0614300)	n.s.	- 0.33 (P = 0.004)	- 0.14 (P = 0.02)	Putative organic anion transporter (Martin et al., 2005)
PMRT1 (PF3D7_1135300)	n.s.	- 0.36 (P = 0.009)	n.s.	Putative transporter at PPM (Wichers et al., 2022)
PLP3 (PF3D7_0923300)	n.s.	- 0.42 (P = 0.015)	n.s.	Host cell permeabilization and rupture (Sassmannshausen et al., 2020)
OSCP (PF3D7_1310000)	n.s.	n.s.	+ 0.58 (P = 0.01)	Subunit of mitochondrial H^+-importing ATP synthase (Gardner et al., 2002)
GFT (PF3D7_0212000)	n.s.	n.s.	+ 0.54 (P = 0.03)	GDP-fucose import, GMP export from Golgi (Martin et al., 2005)
SEC61γ (PF3D7_0210000)	n.s.	n.s.	- 0.23 (P = 0.001)	ER import of proteins destined for export (Marapana et al., 2018)
SEC61β (PF3D7_0821800)	n.s.	n.s.	- 0.31 (P = 0.0005)	ER import of proteins destined for export (Marapana et al., 2018)
DTC (PF3D7_0823900)	n.s.	n.s.	- 0.34 (P = 0.004)	Imports dicarboxylate, exports tricarboxylate from mitochondrion (Gardner et al., 2002)

Putative and known transporter genes were filtered from differentially expressed genes in the described RNA-sequencing experiments using a list of *P. falciparum* transport proteins (Wunderlich, 2022). The log_2 (fold change) of gene expression at the ring stage (6 – 9 hours post invasion) and known or proposed functions are indicated for significantly regulated genes (exact $P < 0.05$). The identified (potential) iron transport proteins are highlighted in red. DV, digestive vacuole; EPM, erythrocyte plasma membrane; PPM, parasite plasma membrane.

(Supplementary Figure S2), indicating the importance of this mitochondrial transporter for asexual parasite growth during the blood stage.

The GFP-tagged mitochondrial carrier protein *Pf*MRS3 exclusively localized to the mitochondrion, as determined by colocalization with MitoTracker Red (Figure 3A, Supplementary Video S1). *Pf*VIT-GFP displayed a punctate fluorescence pattern within the cytoplasm (Figure 3B; Supplementary Video S2), which did not colocalize with ER Tracker Red in live cells (Figure 3B; Supplementary Video S2). Expression of *Pf*ZIPCO-GFP resulted in highly similar fluorescent cytoplasmic dots (Figure 3C; Supplementary Video S3). To test whether these could be acidocalcisomes, we employed LysoTracker Deep Red, commonly used to visualize small acidic organelles in *T. brucei* (Huang et al., 2014). However, the fluorescent dye only stained the DV in *P. falciparum* (Figure 3C; Supplementary Video S3) and no acidocalcisome-specific marker is currently available for this parasite. For both *Pf*VIT-GFP and *Pf*ZIPCO-GFP, the number of cytoplasmic foci increased as the parasites matured from the ring to the late schizont stage (Figures 3B, C).

GFP-tagged *Pf*E140 (PF3D7_0104100), also known as conserved *Plasmodium* membrane protein or CPMP (Lerch et al., 2017), localized to the parasite plasma membrane, as evidenced by the ring-like fluorescence pattern around newly formed merozoites (Figure 3D; Supplementary Video S4). The fluorescence intensity was very low at the ring and early trophozoite stage compared to schizonts. Because of amino acid sequence similarity ($E = 9 \times 10^{-5}$, 22.5% identity, 66% coverage) to the essential apicoplast transporter *Pf*DER1-2 (Altschul et al., 1997; Spork et al., 2009), we also investigated the potential colocalization with the apicoplast marker *Pf*ACP (acyl carrier protein), which could not be detected (Figure 3D; Supplementary Video S4).

3.4 Role of identified proteins for asexual malaria parasite growth

To study the function of the putative transport proteins identified, we used targeted gene disruption (TGD) by selection-linked integration (SLI) to generate the corresponding knockout parasite lines for the putative iron transporters that are non-essential during *P. falciparum* blood stage: *Pf*VIT and *Pf*ZIPCO (Figure 4A; Supplementary Figure S2). The cloning strategy requires a homology region of at least 400 bp, and GFP was cloned in frame with the truncated version of the respective transporter (the N-terminal 143 amino acids (aa) of 274-aa *Pf*VIT or 117 of the 325 aa of *Pf*ZIPCO). The subcellular localization of the resulting GFP fusion protein was also assessed to confirm protein expression and elucidate the position of targeting signals. *Pf*VIT *(1*–143)-GFP localized to cytoplasmic structures and *Pf*ZIPCO(1-117)-GFP to the DV and cytoplasmic vesicles (Figure 4A). Hence, both truncated proteins contained (a) sequence(s) for targeting to the observed vesicles. As additional DV staining is often non-specific, another part of the protein located within the C-terminal 208 aa of *Pf*ZIPCO may be required for exclusively vesicular localization.

TABLE 2 Proteins identified by RNA-sequencing that may be involved in iron transport in *P. falciparum*.

Gene product, gene ID	Blood stage transcription peak	classification	Solved structure of a similar protein	Potential human ortholog(s)	Localization in *P. falciparum*	Transport assays and proposed function	Mutability in *P. falciparum*	Essentiality in *P. berghei*
MRS3, PF3D7_0905200	20 hpi	2.A.29.5.9	None	Mitoferrin-1 ($E = 7 \times 10^{-10}$, 27.0% identity, 26% coverage); Mitoferrin-2 ($E = 6 \times 10^{-8}$, 27.9% identity, 12% coverage)	Mitochondrion (this study)	Liposomal transport assays with *S. cerevisiae* MRS3 (Brazzolotto et al., 2014): Fe^{2+} import into mitochondrial matrix across inner membrane	Non-disruptable, MIS: 0.135 (Zhang et al., 2018)	PBANKA_041620: essential at asexual blood stage (Bushell et al., 2017)
VIT, PF3D7_1223700	36 hpi	2.A.89.1.13	Crystal structure of VIT1 from *Eucalyptus grandis*: PDB: 6IU9 (Kato et al., 2019)	None	Cytoplasmic vesicles (this study)	Transport assays using inverted vesicles with *Pf*VIT (Labarbuta et al., 2017): Fe^{2+} export from cytosol into cytoplasmic vesicles (this study) in exchange for H^+	Disruptable, MIS: 0.903 (Zhang et al., 2018)	PBANKA_143860: dispensable at asexual blood stage with growth rate of 1 (95% CI: 0.94 – 1.05) (Bushell et al., 2017), and at mosquito and liver stage (Stanway et al., 2019); reduced growth in blood and liver in mice (Slavic et al., 2016)
ZIPCO, PF3D7_1022300	32 hpi	2.A.5.3.12	Cryo-EM structure of ZIP from *Bordetella bronchiseptica*, PDB: 8GHT (Pang et al., 2023)	ZIP1 ($E = 2 \times 10^{-5}$, 21.7% identity, 48% coverage)	Cytoplasmic vesicles (this study)	Zn^{2+} uptake assays with *Bb*ZIP in *Escherichia coli* (Pang et al., 2023), Liposomal assays with *Pf*ZIP1 (Shrivastava et al., 2024): Fe^{2+}/Zn^{2+} import into cytosol from cytoplasmic vesicles (this study)	Disruptable, MIS: 1 (Zhang et al., 2018), growth increase at asexual blood stage (this study)	PBANKA_050650: growth rate of 0.86 (95% CI: 0.74 – 0.98) at asexual blood stage (Bushell et al., 2017); dispensable at blood and mosquito stages but reduced sporozoite infectivity and inefficient liver schizogony in mice (Sahu et al., 2014)
NRAMP, PF3D7_0523800	14 hpi	2.A.55.2.25	Crystal structure of NRAMP/DMT from *Staphylococcus capitis*, PDB: 5M95 (Ehrnstorfer et al., 2014)	NRAMP1 ($E = 2 \times 10^{-38}$, 28.4% identity, 56% coverage); NRAMP2 ($E = 2 \times 10^{-38}$, 27.6% identity, 65% coverage)	DV (Wichers et al., 2022)	Uptake assays with *Deinococcus radiodurans* NRAMP in *E. coli* and proteoliposomes (Bozzi et al., 2016; Bozzi et al., 2019): pH-dependent symport of Mn^{2+}/Fe^{2+} with H^+ into cytosol from DV	Non-disruptable, MIS: 0.123 (Zhang et al., 2018)	PBANKA_123860: no mutants generated

(Continued)

10.3389/fcimb.2024.1480076

TABLE 2 Continued

Gene product, gene ID	Blood stage transcription peak	classification	Solved structure of a similar protein	Potential human ortholog(s)	Localization in *P. falciparum*	Transport assays and proposed function	Mutability in *P. falciparum*	Essentiality in *P. berghei*
CRT, PF3D7_0709000	14 hpi	2.A.7.20.1	Cryo-EM structure of *Pf*CRT from strain 7G8, PDB: 6UKJ (Kim et al., 2019)	None	DV (Kuhn et al., 2010)	Transport assays using *Xenopus* oocytes with *Pf*CRT (Bakouh et al., 2017): symport of Fe^{2+} with H^+ into cytosol from DV	Non-disruptable, MIS: 0.127 (Zhang et al., 2018), essential at asexual blood stage (Waller et al., 2003)	PBANKA_121950: essential at asexual blood stage (Ecker et al., 2011; Bushell et al., 2017)
E140, PF3D7_0104100	40 hpi	Unknown	None	None	PPM (this study)	Putative Fe^{2+} importer at PPM (this study)	Non-disruptable, MIS: 0.119 (Zhang et al., 2018)	PBANKA_0209000: growth rate of 0.48 (95% CI: 0.32 – 0.63) at asexual blood stage (Bushell et al., 2017), dispensable in mosquito and liver stages (Stanway et al., 2019)

The transcription peaks are indicated as in Broadbent et al. (2015) and the classification of the proteins identified according to the Transport Classification Database (Saier et al., 2016). Data on human orthologs was retrieved using the NCBI position-specific iterated (PSI) BLAST with default settings at https://blast.ncbi.nlm.nih.gov/Blast.cgi (Altschul et al., 1997). DV, digestive vacuole; E, expect value; EM, electron microscopy; hpi, hours post invasion; MIS, mutagenesis index score; PDB, Protein Data Bank; PPM: parasite plasma membrane.

Proliferation assays were then performed to determine the importance of the respective transporter for parasite growth. While the *Pf*VIT knockout had no effect on parasite growth under standard conditions, addition of hepcidin reduced the growth rate of the ΔVIT line by 30% (Figure 4B). Of note, hepcidin generally had a smaller effect after two cycles of incubation (Figure 4B) than after one cycle compared to the first IDC (Figure 1B). Unexpectedly, knocking out *Pf*ZIPCO led to a growth rate increase by 42% after two IDCs relative to wild-type 3D7 parasites, and thus a rescue by hepcidin treatment was not tested for this knockout line (Figure 4B).

*Pf*E140 is predicted to be essential (Zhang et al., 2018) and the only putative iron transporter identified that localized to the PPM (Figure 3), thus potentially important for iron uptake in *P. falciparum*. For an inducible knockdown, a *glmS* ribozyme sequence (Prommana et al., 2013) was introduced upstream of the 3' untranslated region in the pSLI plasmid, allowing for conditional mRNA degradation by adding 2.5 mM glucosamine (GlcN) to the culture medium (Figure 4C; Supplementary Figure S2). The knockdown led to a 61% decrease in total parasite fluorescence intensity after 36 hours of GlcN treatment (Figure 4D) without affecting parasite size compared to untreated control (Figure 4E). Addition of GlcN also caused a 38% growth rate reduction of the *Pf*E140-GFP-*glmS* line, which was rescued by hepcidin treatment to a proliferation level that was not significant different from that under standard culture conditions ($P = 0.25$, Figure 4F). The generation of a *Pf*MRS3-knockdown line was not successful after four independent attempts of G418 selection for integrants after transient transfection, supporting the essentiality of the gene for asexual parasite growth (Zhang et al., 2018).

3.5 Functional implications of predicted transport protein structures

We next took advantage of the recent progress in protein structure prediction and generated models of the putative iron transport proteins identified (Table 2) using AlphaFold2 (Jumper et al., 2021; Varadi et al., 2022) and AlphaFold2-multimer (Evans et al., 2022). The transmembrane regions of the proteins typically exhibited the highest confidence score, while some other protein portions appeared unstructured (Figure 5A). Regions that are likely located within a membrane were validated by inspecting the molecular lipophilicity potential of the protein surfaces (Figure 5B). A clear hydrophobic belt was observed for all proteins and their orientation in the membrane was determined on the basis of orthologous proteins. As transport cavities with negatively charged residues are a hallmark of heavy metal ion transporters, we analyzed the distribution of charge on the surface of the proteins and looked for negatively charged regions to assess the capacity to bind cations like Fe^{2+} (Figure 5C). To gain further insights into the functions of the proteins identified, we also compared the predicted structures with those of well-characterized homologs from *S. cerevisiae*, *Eucalyptus grandis, Bordetella bronchiseptica* and *Staphylococcus capitis* (Table 2; Supplementary Figures S3, S4).

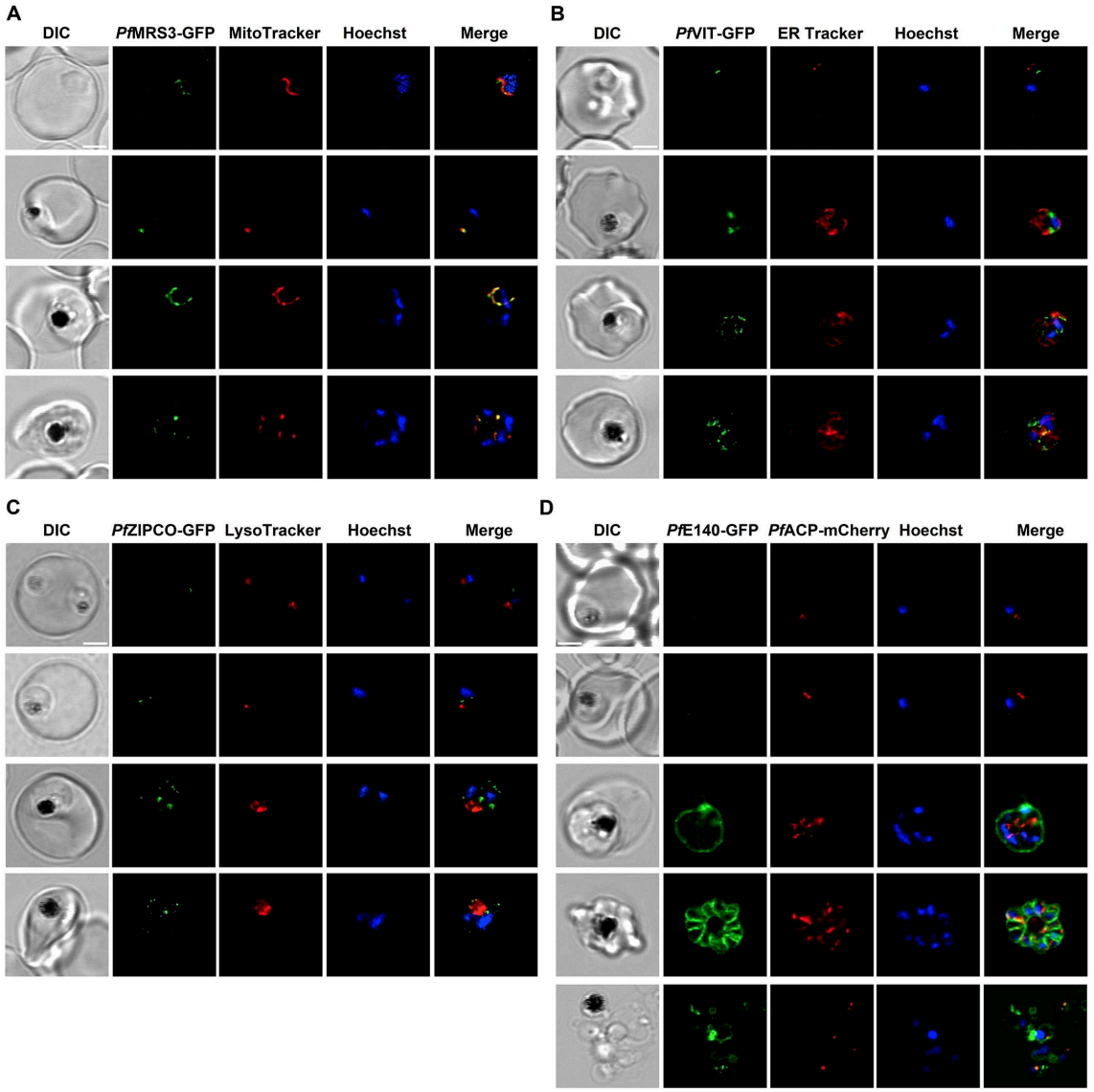

FIGURE 3
Subcellular localization of known and putative iron transport proteins. Representative erythrocytes infected with *P. falciparum* 3D7 parasites endogenously expressing GFP-tagged *Pf*MRS3 **(A)**, *Pf*VIT **(B)**, *Pf*ZIPCO **(C)** or *Pf*E140 **(D)** were additionally stained with the fluorescent dyes Hoechst-33342, MitoTracker Red, ER Tracker Red and/or LysoTracker Deep Red. Co-transfection with a construct that encodes the 60 N-terminal amino acids of acyl carrier protein (*Pf*ACP) tagged with mCherry (Birnbaum et al., 2020) resulted in red fluorescence of the apicoplast. Live-cell images were taken under physiological conditions at 37°C using an SP8 confocal laser-scanning microscope (Leica). DIC, differential interference contrast. Scale bar, 2 µm.

The outer surface of *Pf*MRS3 (transport classification (TC): 2.A.29, mitochondrial carrier family) is positively charged (Figure 5C) and there is a clear negatively charged patch in the putative binding pocket facing the mitochondrial intermembrane space. We compared the predicted *Pf*MRS3 structure with that of *S. cerevisiae* MRS3, which is known to import ferrous iron into the mitochondrial matrix across the inner membrane (Mühlenhoff et al., 2003; Froschauer et al., 2009; Brazzolotto et al., 2014). The predicted structures of *Pf*MRS3 and *S. cerevisiae* MRS3 were superimposed with an average root mean square deviation of Cα atoms (Cα RMSD) of the 205 matched residues of 2.3 Å (Supplementary Figures S3A, S4A). The conserved histidine residues His^{48} and His^{105} that were required for Fe^{2+} transport by *S. cerevisiae* MRS3 in reconstituted liposomes (Brazzolotto et al., 2014) are also present in *Pf*MRS3 and are in a similar molecular context in both structures (Supplementary Figures S3A, S4A). This suggests that MRS3 may elicit similar molecular functions in *S. cerevisiae* and *P. falciparum*.

*Pf*VIT is highly similar to VIT1 from *E. grandis* ($E = 7 \times 10^{-27}$, 30.3% identity, 84% coverage), for which an experimental structure is available (Protein Data Bank (PDB) identifier: 6IU4). The plant protein crystallized as a homodimer (Kato et al., 2019), and the same oligomeric state was suggested for the vacuolar iron transporter family (TC: 2.A.89) protein in *P. falciparum* (Sharma et al., 2021). A *Pf*VIT monomer also has five transmembrane domains and comprises a negatively charged region facing the

10.3389/fcimb.2024.1480076

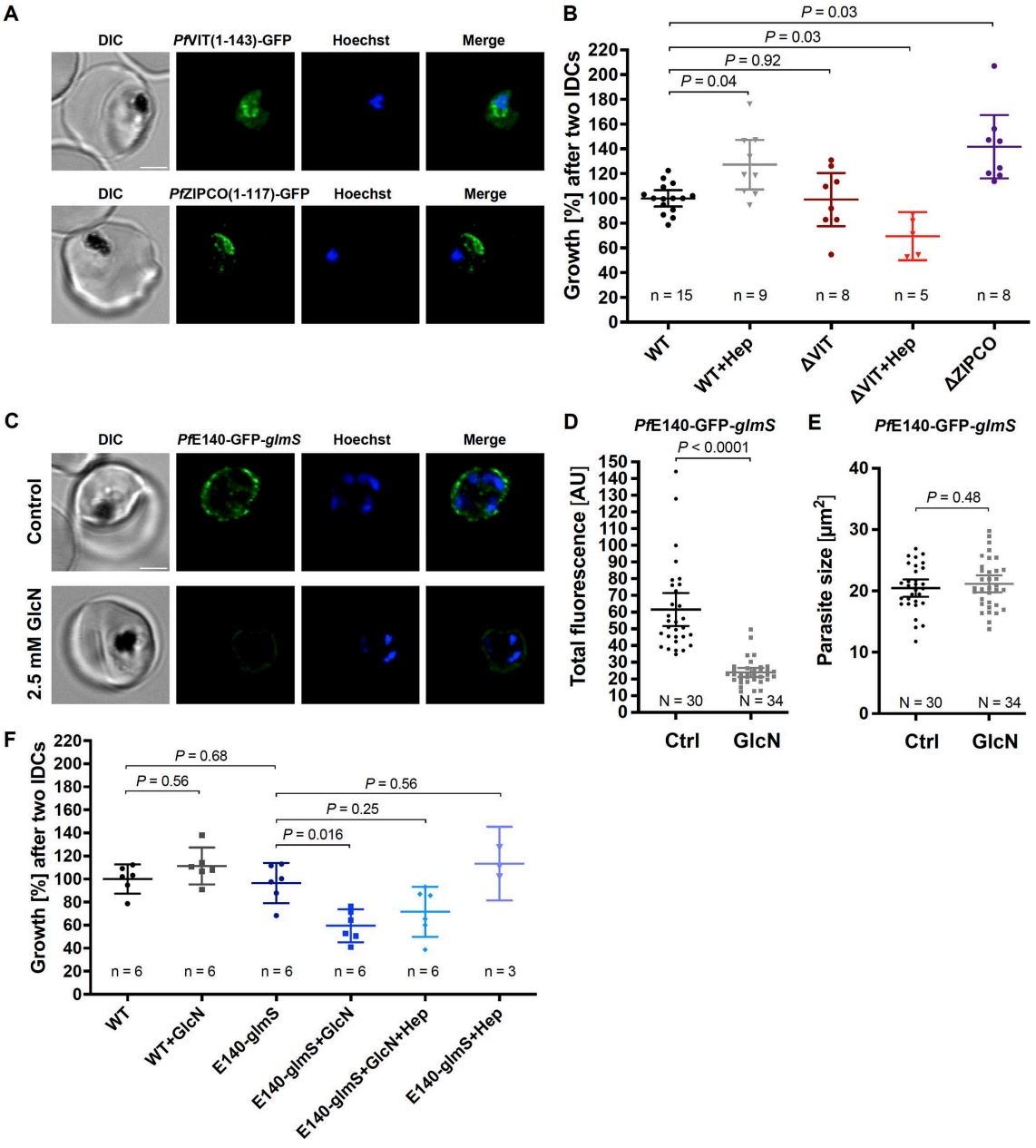

FIGURE 4
*Pf*VIT and *Pf*E140 are important for *P. falciparum* growth and may be involved in intracellular iron homeostasis. **(A)** Representative erythrocytes infected with *P. falciparum* 3D7 parasites that endogenously express a truncated version of *Pf*VIT or *Pf*ZIPCO tagged with GFP (green). **(B)** Growth rates of knockout parasite lines generated. **(C)** Representative live 3D7 parasites endogenously expressing *Pf*E140-GFP whose green fluorescence was reduced by *glmS*-mediated knockdown induced by treatment with 2.5 mM glucosamine for 36 h (GlcN) compared to untreated control (Ctrl). **(D)** Total parasite fluorescence intensities were quantified as background-corrected integrated densities using ImageJ version 2.9.0/1.53t (Schindelin et al., 2012) and compared using Mann-Whitney test. Images to which no averaging or deconvolution software was applied were used for quantification. **(E)** The size of the parasites was measured as the area of the region of interest and compared using equal variance unpaired *t* test. **(F)** Conditional knockdown of *Pf*E140 induced by treatment with 2.5 mM GlcN results in a growth defect during asexual blood stage development. Live parasites were stained with Hoechst-33342 (blue) and imaged under physiological conditions at 37°C using an SP8 confocal laser-scanning microscope (Leica). DIC, differential interference contrast. Scale bar, 2 µm. Error bars represent 95% confidence intervals of the mean, N the number of parasites analyzed, n the number of independent experiments and Hep treatment with 0.7 µM hepcidin. Growth rates refer to the fold change in parasitemia after two intraerythrocytic developmental cycles *in vitro* relative to untreated wild-type 3D7 parasites (WT) as determined by flow cytometry with SYBR Green I (Malleret et al., 2011). Statistical significance of growth differences was calculated with two-tailed unpaired *t* tests with Welch's correction for unequal variances and adjusted with the Holm-Šídák method for multiple comparisons.

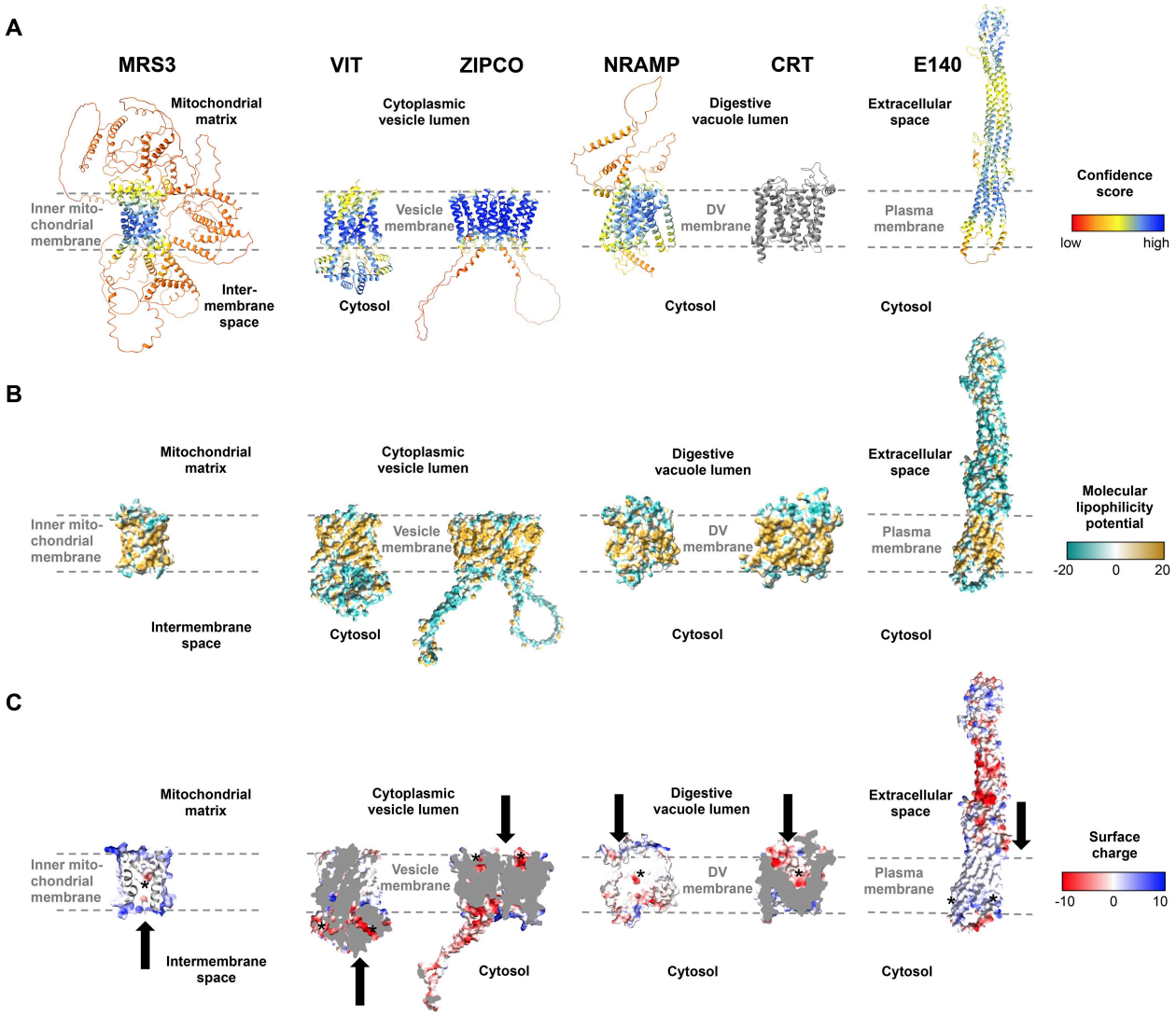

FIGURE 5
Structures of known and putative *P. falciparum* iron transporters as viewed from the membrane plane. **(A)** Predicted protein structures with per-residue pLDDT (predicted local distance difference test) confidence scores on a scale from 0 to 100, where blue represents high and red low confidence, respectively. The experimentally determined structure of *Pf*CRT is shown in gray. **(B)** Molecular lipophilicity potential of the protein surfaces as implemented in UCSF ChimeraX; tan is hydrophobic and cyan hydrophilic. Dashed lines above and below the tan regions of all proteins indicate the respective membrane and disordered loops were removed for clarity. **(C)** Surface charge of the proteins with positively charged areas colored blue and negatively charged ones red. Putative cation-binding site are indicated with an asterisk and transport directions by arrows. *Pf*E140 likely forms a dimer but is shown as a monomer, as no predicted dimer structure could be obtained using AlphaFold2-multimer. The putative cation-binding sites for this protein are based on DeepFRI gradCAM scores for the functional term GO:0015075 "monoatomic ion transmembrane transporter activity" (Supplementary Figure S5).

cytosol that may enable cation transport (Figure 5C). In agreement with this, one Fe^{2+} ion and two Zn^{2+} ions were bound by a strongly charged region on the cytosolic side of the *E. grandis* VIT1 monomer (Kato et al., 2019) and a highly similar putative binding pocket is present in the parasite protein (Supplementary Figure S4B). In the structural alignment, 219 of the 227 residues of the experimental *Eg*VIT1$^{23\text{-}249}$ structure are within 5 Å of the predicted structure of *Pf*VIT with an average Cα RMSD of 1.9 Å and the key residues in the metal-binding domain (Glu^{102}, Glu^{105}, Glu^{113}, Glu^{116}, using *Eg*VIT1$^{23\text{-}249}$ numbering) are placed in a similar molecular context in the predicted structure of *Pf*VIT (Supplementary Figures S3B, S4B). The residues in the transmembrane domain that are in the vicinity of the Co^{2+} ion in the *Eg*VIT1$^{23\text{-}249}$ structure (Met^{80} and Asp^{43}) are also conserved (Supplementary Figure S3B), which is in line with a similar function of *Pf*VIT and *Eg*VIT1.

*Pf*ZIPCO contains seven transmembrane domains and was modeled as a homodimer (Figure 5A), as it is part of the zinc (Zn^{2+})-iron (Fe^{2+}) permease (ZIP) family (TC: 2.A.5), whose members usually function as homo- or heterodimers (Saier et al., 2016). The negatively charged patch in each binding pocket facing the vesicle lumen (Figure 5C) may be involved in cation transport to the cytosolic side. In an overlay of the *Pf*ZIPCO model with the cryo-EM structure (PDB: 8GHT) of a ZIP transporter from *B.*

bronchiseptica in the presence of either Zn^{2+} or Cd^{2+} ions (Pang et al., 2023), the average Cα RMSD of 140 sequence-aligned residues was 2.0 Å (Supplementary Figures S3C, S4C). Several key residues of the metal binding site M1 of *Bb*ZIP (Met^{99}, His^{177}, Glu^{181}, Glu^{211}) were also found in *Pf*ZIPCO, whereas others (Asn^{178}, Gln^{207}, Asp^{208}, Glu^{240}) were different (Supplementary Figure S3C), possibly resulting in divergent substrate specificity.

*Pf*NRAMP (TC: 2.A.55, metal ion (Mn^{2+}-iron) transporter family) is a homolog of the human endosomal Fe^{2+} transporter 2/DMT1 (Martin et al., 2005) and contains twelve transmembrane domains (Figure 5A). Like *Pf*CRT (TC 2.A.7, drug/metabolite exporter family), for which a recent cryo-EM structure (PDB: 6UKJ) is available (Kim et al., 2019), the predicted structure possesses a negatively charged region within its binding pocket facing the digestive vacuolar lumen (Figure 5C). This is consistent with binding of cations such as Fe^{2+}. The *Pf*NRAMP model was superimposed on the solved crystal structure of *S. capitis* NRAMP/DMT (PDB: 5M95, $E = 1 \times 10^{-32}$, 26.3% identity, 60% coverage), which was shown to bind Mn^{2+}, Fe^{2+}, Co^{2+}, Ni^{2+}, Cd^{2+} and Pb^{2+} (Ehrnstorfer et al., 2014). In the overlay, the average Cα RMSD of the 349 matched residues was 1.6 Å and the negatively charged cavity of *Pf*NRAMP was in close proximity to the Mn^{2+} ion bound to *S. capitis* NRAMP (Supplementary Figure S3D, Supplementary Figure S4D). Two of the four key residues required for ion coordination in the binding pocket of the bacterial protein (Asn^{52} and Asp^{49}) are present in *PfNRAMP*, whereas the two other residues (Met^{226} and Ala^{223}) are changed to serine. The functional implications of the latter are unclear; Ehrnstorfer et al (Ehrnstorfer et al., 2014) showed that Met^{226}Ala mutant of *S.capitis* NRAMP exhibited reduced transport activity and binding, however, transport could not be completely abolished by these mutations. While potential effects of these differences on substrate specificity and/or transport activity remain to be elucidated, *Pf*NRAMP is likely to perform cation transport from the DV into the cytosol.

*Pf*E140 is predicted to be anchored in the parasite plasma membrane by a bundle of five transmembrane domains (Meerstein-Kessel et al., 2021). In the AlphaFold prediction, it forms a coiled coil with a hydrophilic region that displays negatively charged patches exposed to the extracellular side (Figures 5A, B). No human orthologs could be identified for this highly conserved *Plasmodium* protein (Altschul et al., 1997). As there is no obvious channel or cavity in the transmembrane region of the *Pf*E140 monomer (Figures 5B, C), the helical bundles may form a dimer to enable ion transport. However, we were not able to obtain a *Pf*E140 dimer model with AlphaFold2-multimer because of its sequence length. To predict functional residues on the basis of the amino acid sequence and the AlphaFold2 structure of *Pf*E140, we used DeepFRI graph convolutional network (Gligorijević et al., 2021), which has significant denoising capability and can reliably assign GO terms to residues in the protein. In particular, the terms GO:0022857 "transmembrane transporter activity" (DeepFRI gradCAM score 0.94), GO:0015075 "monoatomic ion transmembrane transporter activity" (score 0.78), and GO:0046873 "metal ion transmembrane transporter activity" (score 0.67) were assigned to a putative transmembrane region of *Pf*E140 with high confidence (Supplementary Figure S5). We thus speculate that the protein is a transporter of metal ions.

4 Discussion

Here, we studied the role of iron in growth and transcription of *P. falciparum* by using blood from individuals of different iron status and by adding hepcidin as an iron-regulatory hormone and ferroportin inhibitor. Overall, our data demonstrate the importance of Fe^{2+} in parasite replication and development and highlight areas for further study. We showed that *in vitro* growth rates of *P. falciparum* 3D7 and the number of merozoites formed per schizont were reduced within erythrocytes that contain lower concentrations of labile iron, while culturing in blood from an individual with higher iron status did not lead to a significant increase in labile iron levels within erythrocytes or in parasite growth relative to control (Figure 1). Consistent with this, reduced propagation of *P. falciparum* 3D7, Dd2, and FCR3-FMG was reported when erythrocyte samples from iron-deficient individuals used for parasite culture (Clark et al., 2014; Goheen et al., 2017). This effect was eliminated after these donors were iron-supplemented, whereas supplementation of healthy (iron-replete) donors did not significantly promote parasite growth (Clark et al., 2014). The strong increase in parasite replication in the presence of hepcidin relative to control conditions (Figure 1B) may have been a result of enhanced invasion efficiency in addition to the increased number of merozoites formed (Figure 1D). Earlier studies also found that higher hepcidin levels in blood samples were associated with elevated *P. falciparum* growth rates *in vitro* (Goheen et al., 2017) and severe malaria *in vivo* (Muriuki et al., 2021), however, the effect of experimental hepcidin addition on parasite growth had not been assessed previously.

To identify putative iron transporters and iron-regulated processes, we carried out RNA-sequencing analyses of *P. falciparum* during the ring and trophozoite stages cultured under the different iron conditions described above. A higher number of biological processes and pathways were significantly enriched among DEGs when erythrocytes from donors with different iron status were used for parasite culture (Figure 2C) compared to red blood cells from the same healthy donor in the presence vs. absence of hepcidin (total of 28 vs. 13 functional terms, Figure 2E). This may reflect greater differences in the culture conditions; for instance, blood from the donor with high serum ferritin and Hb levels may have also contained more glucose or copper (Newhouse et al., 1993; Kim et al., 2011), potentially explaining the more diverse physiological response of the parasite. Including erythrocyte samples from more individuals in the growth experiments and RNA-sequencing analysis would have provided further insights, however, the provision of sufficient blood from iron-deficient donors is limited by ethical constraints.

The availability of additional nutrients likely resulted in increased endocytosis and digestion of host cell contents in the DV of the parasite, leading to enhanced metabolism, mRNA splicing, and protein production. Interestingly, the terms KEGG:01100 "metabolic pathways" and GO:0005737 "cytoplasm" were also found to be enriched in upregulated parasite genes in children with high vs. low parasitemia (Milner et al., 2012; Thomson-Luque et al., 2021). RNA binding and mRNA splicing processes were previously reported to be overrepresented in

upregulated genes in severe malaria linked to high parasite density (Milner et al., 2012; Lee et al., 2018; Thomson-Luque et al., 2021). Hence, an increase in overall parasite fitness under high vs. low-iron conditions may explain the increase in parasite multiplication (Figure 1B) and could be associated with higher parasitemia and disease severity. Consistent with the observed upregulation of transmembrane transporters at 6 – 9 hpi under high vs. low-iron conditions, Mancio-Silva et al. found that the functional term "ion transporter activity" was enriched in *P. berghei* genes that were downregulated under caloric restriction at 6 and 10 hpi (Mancio-Silva et al., 2017). Thus, transmembrane transporter genes may need to be transcribed at the beginning of the IDC to ensure that the appropriate level of transport proteins is available for nutrient acquisition and metabolite efflux during the subsequent metabolically active trophozoite and schizont stages.

Hepcidin plays a central role in mammalian iron homeostasis and reduces serum iron concentrations (Muckenthaler et al., 2017). It is also known that hepcidin levels are elevated in *P. falciparum*-infected individuals, especially those with high parasitemia (Cercamondi et al., 2010; Muriuki et al., 2021), and that malaria causes iron deficiency (Muriuki et al., 2021). The transcription profile of parasites treated with 0.7 µM hepcidin showed similarities to those cultured in erythrocytes from the iron-deficient donor compared to standard conditions in terms of downregulated catabolic and translation processes as well as transport protein regulation (Figure 2; Table 1). This may be related to the fact that an aberrant hepcidin increase causes systemic iron deficiency as a result of restricted iron availability (Ginzburg, 2019). The upregulation of genes involved in merozoite motility (*Pf*MTIP, *Pf*GAP45, and various inner membrane complex proteins) and host cell entry (such as *Pf*AMA1, *Pf*MSP3, *Pf*MSP7, and *Pf*EBA181) when hepcidin was present (Figure 2) may suggest an improved ability of the released merozoites to invade erythrocytes. Thus, the addition of the peptide hormone to the culture media could be a signal for the parasite to reduce metabolic processes and to increase its invasion efficiency.

In addition to roles in parasite proliferation and development, different levels of labile iron may induce regulatory processes at various levels. Under high-iron conditions, the observed upregulation of histone deacetylation (Figure 2C) may lead to the condensation and thus deactivation of certain chromatin regions (Duraisingh and Skillman, 2018). The binding sites and target genes of the differentially expressed transcription factors and of *Pf*IRP remain to be identified in *P. falciparum*. Moreover, protein phosphorylation may play a role in iron-dependent regulatory mechanisms. As a serine/threonine kinase (KIN) serves as a nutrient sensor in *P. berghei*, driving a fast response that leads to increased parasite multiplication and virulence (Mancio-Silva et al., 2017), a similar kinase may sense iron and lead to increased replication in *P. falciparum*.

On the basis of our RNA-sequencing results (Figure 2, Table 1) and the *P. falciparum* transporter list (Wunderlich, 2022), we identified six proteins that are likely involved in iron transport in the parasite (Table 2; Figure 6) and analyzed their subcellular localization (Figure 3), their importance for growth (Figure 4), and their predicted structures (Figure 5). *Pf*MRS3 transcription was upregulated at the ring stage under high vs. low-iron conditions ($\log_2$ FC = 0.33, P = 0.002, Figure 2B), and fluorescence of the GFP-tagged protein was exclusively detected at the mitochondrion (Figure 3A). As a disruption of the gene was reported to fail (Zhang et al., 2018), and parental DNA of the original gene locus was still present in the GFP reporter line (Supplementary Figure S2), *Pf*MRS3 is likely essential for asexual growth like PBANKA_041620 (E = 1 x 10^{-69}, 71.4% identity, 25% coverage) in *P. berghei* (Bushell et al., 2017). A knockdown of the gene could not be evaluated because we were not able to select stable integrants with G418 after transient transfection of the *glmS* construct upon four independent attempts. Thus, the parasite may not tolerate an insertion of the *glmS* sequence into its genome, as this can already lead to a slight gene knockdown even without glucosamine addition to the culture media. The orthologous mitochondrial iron transporter (*Tg*MIT, TGME49_277090, E = 7 x 10^{-19}, 26.0% identity, 28% coverage) also localized to the mitochondrion in *T. gondii* and was upregulated at the protein level upon iron overload in consequence of a *Tg*VIT knock out in the related apicomplexan parasite (Aghabi et al., 2023). Our structural analyses (Figure 5; Supplementary Figures S3A, S4A) further support that *Pf*MRS3 imports ferrous iron into the mitochondrion, the main iron user of the cell, thereby reducing the cytosolic Fe^{2+} concentration (Figure 6) as a means of detoxification, which has been reported for yeast (Li et al., 2010). The protein's substrate specificity as well as its iron- binding and transport activities remain to be confirmed experimentally.

Complementation assays in *S. cerevisiae* indicated a role for *Pf*VIT in iron detoxification (Slavic et al., 2016; Sharma et al., 2021) and we observed that the expression of the gene was upregulated under high vs. low-iron conditions in *P. falciparum* ($\log_2$ FC = 0.29, P = 0.02, Figure 2B). The fluorescence pattern of *Pf*VIT-GFP in live cells (Figure 3B) was consistent with cytoplasmic vesicles that may be acidocalcisomes, as described for *T. brucei* VIT1 (Huang et al., 2014). An increase in the number of fluorescent punctate structures during parasite development (Figure 3B) was also observed for VIT in *T. gondii* (Aghabi et al., 2023). *Pf*VIT shares 47.0% identity with *Tg*VIT (E = 8 x 10^{-84}, 95% coverage) and 36.9% identity with *Tb*VIT1 (E = 9 x 10^{-39}, 98% coverage). In contrast, *P. berghei* VIT (PBANKA_143860, E = 3 x 10^{-160}, 79.3% identity, 98% coverage) was shown to localize to the ER in indirect immunofluorescence assays (Slavic et al., 2016). This may be explained by differences between species or variation in methodology such as fixation, permeabilization, and immunolabeling techniques as opposed to live-cell imaging (Schembri et al., 2007; Schnell et al., 2012; Mathew et al., 2021).

Transport assays using inverted vesicles that were prepared using recombinant *Pf*VIT expressed in *E. coli* demonstrated that the protein is a Fe^{2+}/H^+ antiporter (Labarbuta et al., 2017). The translocation of Fe^{2+} in exchange for H^+ is likely fueled by the pH gradient across the membrane of the acidic vesicles and the high similarity of the putative Fe^{2+}-binding pocket at the cytosolic side of the predicted *Pf*VIT structure with that of experimentally characterized *Eg*VIT1 (Figure 5; Supplementary Figure S4B) provide further evidence for our hypothesis. While not essential during asexual blood stages (Zhang et al., 2018), a knockout of VIT resulted in reduced liver stage development in *P. berghei* (Slavic et al., 2016) and increased sensitivity to high iron levels in both *P.*

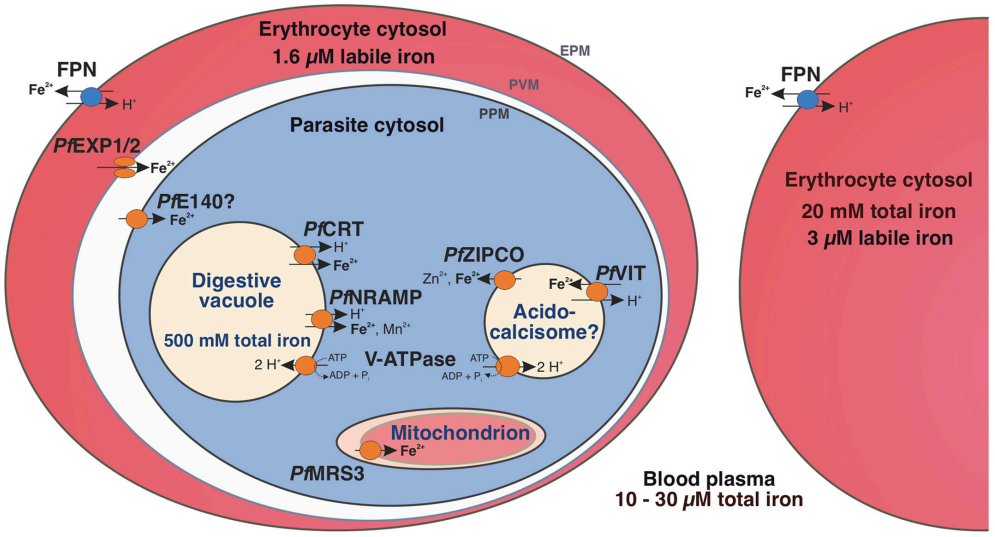

FIGURE 6
Iron homeostasis in a *P. falciparum*-infected erythrocyte. The human blood plasma contains between 10 and 30 μM total iron and the erythrocyte cytosol approximately 20 mM (Egan et al., 2002). However, the labile iron pool is only 3 μM in an uninfected erythrocyte and 1.6 μM in a *P. falciparum*-infected one (Loyevsky et al., 1999). Human ferroportin (FPN) at the host cell surface (erythrocyte plasma membrane, EPM) exports ferrous iron from the erythrocyte (Ward and Kaplan, 2012) and the nutrient pore formed by *Pf*EXP1 and *Pf*EXP2 allows the passage of ions through the parasitophorous vacuole membrane (PVM) (Mesén-Ramírez et al., 2021). *Pf*E140 at the parasite plasma membrane (PPM) may mediate iron uptake into the parasite cytosol and the mitochondrial carrier protein *Pf*MRS3 likely translocates Fe^{2+} into the mitochondrion, a site of *de novo* heme biosynthesis (this study). We propose that the vacuolar iron transporter (*Pf*VIT) is involved in iron detoxification by transporting excess Fe^{2+} from the cytosol into cytoplasmic vesicles that may be acidocalcisomes, whereas *Pf*ZIPCO releases Fe^{2+} from these organelles under low-iron conditions. The digestive vacuole (DV) contains a high amount of total iron as it is the site of hemoglobin degradation and hemozoin formation (Becker et al., 2004). The chloroquine resistance transporter (*Pf*CRT) and the natural resistance-associated macrophage protein (*Pf*NRAMP, also called *Pf*DMT1 for divalent metal transporter 1) were suggested to mediate proton-coupled export of Fe^{2+} from the DV into the parasite cytosol (Martin et al., 2005; Bakouh et al., 2017). Both acidocalcisomes and the DV are likely acidified by the plant-like H^+-pump V-ATPase, which can fuel secondary active transport processes (Wunderlich et al., 2012; de Oliveira et al., 2021). Parasite-encoded proteins are shown in orange and human-encoded transporters in blue.

berghei (Slavic et al., 2016) and *T. gondii* (Aghabi et al., 2023). Similarly, growth of the ΔVIT *P. falciparum* line was not affected under standard conditions, whereas the addition of hepcidin – which increases intracellular labile iron levels (Figure 1A) – compromised parasite proliferation in our study (Figure 4B). Thus, we hypothesize that the transporter sequesters Fe^{2+} into cytoplasmic vesicles, which is important for iron detoxification under high-iron conditions. While ΔVIT *P. falciparum* is more sensitive to elevated intracellular Fe^{2+} concentrations (Figure 4B) as a consequence of impaired removal of excess iron from the cytosol, *Pf*MRS3 may compensate for a loss of *Pf*VIT under standard conditions by transporting ferrous iron from the cytosol into the mitochondrion (Figure 6).

In contrast to the PPM staining of *P. berghei* sporozoites in immunofluorescence assays, *Pf*ZIPCO-GFP expression resulted in a punctate fluorescence pattern in the cytoplasm of live blood-stage *P. falciparum* (Figure 3C), similar to that of *Pf*VIT-GFP (Figure 3B). Whereas the *Pf*ZIPCO knockout caused a growth increase under standard conditions (Figure 4B), ΔZIPCO *P. berghei* parasites displayed normal blood-stage development but impaired sporozoite infectivity as well as reduced replication at the liver stage in mice (Sahu et al., 2014). Interestingly, the ortholog TGME49_225530 is also dispensable in *T. gondii* tachyzoites with a phenotype score of −2.94 (values below -1.5 are considered non-essential (Sidik et al., 2016)). Hence, Fe^{2+} efflux from cytoplasmic vesicles (potentially acidocalcisomes) into the cytosol via *Pf*ZIPCO may be dispensable in *P. falciparum* under iron-replete conditions during the blood stage because of the redundancy with iron import mechanisms into the parasite, and the production of the protein may result in a fitness cost. In contrast, liver-stage parasites in low-iron environments may rely on the transporter's activity when the demand for iron is high during schizogony. As the transcription of *Pf*ZIPCO was upregulated at low vs. control iron levels (log_2 FC = 0.55, $P = 0.04$, Table 1) and in response to hepcidin treatment (log_2 FC = 0.63, $P = 0.006$, Figure 2D; Table 1), the transport protein may release Fe^{2+} and Zn^{2+} ions from intracellular stores, in this case cytoplasmic vesicles (Figure 6), in case of scarcity, thereby increasing cytosolic ion levels like other ZIP transporters (Sloan et al., 2021). While our analyses of the predicted structure and its alignment with *Bb*ZIP indicate that *Pf*ZIPCO likely has the capacity to bind and transport cations like Fe^{2+} or Zn^{2+} (Figure 5; Supplementary Figures S3C, S4C), its substrate specificity can only be conclusively established by characterizing the purified protein. Liposomal assays with the putative zinc transporter *Pf*ZIP1 (PF3D7_0609100, 24.5% identity with *Pf*ZIPCO, E = 1 x 10^{-19}, 78% coverage), which localized to the plasma membrane in schizonts, demonstrated that this ZIP transporter preferentially binds Zn^{2+} over Fe^{2+} (Shrivastava et al., 2024). Interestingly, this preference was abolished if the histidine-rich loop at the C-terminus of *Pf*ZIP1, which is not present in *Pf*ZIPCO, was truncated. As

mRNA levels of *Pf*ZIP1 were enhanced at low cytosolic Zn^{2+} levels (Shrivastava et al., 2024) but not differentially regulated under various iron conditions (Supplementary Tables S1, S2), it may play a role in zinc rather than iron homeostasis under physiological conditions.

As the highest intracellular iron concentration in *P. falciparum* is reached within the DV (Becker et al., 2004; Rohrbach et al., 2005), the free form of the metal may need to be exported from this compartment under high-iron conditions to prevent damage to the DV membrane (Figure 6). This function may be fulfilled by *Pf*CRT (Bakouh et al., 2017) and/or *Pf*NRAMP (Martin et al., 2005), which were both upregulated under high vs. low-iron conditions in our RNA-sequencing analysis ($\log_2$ FC = 0.26, P = 0.007 and $\log_2$ FC = 0.28, P = 0.003, respectively, Figure 2B, Table 1) and are essential in asexual parasites (Waller et al., 2003; Zhang et al., 2018; Wichers et al., 2022). The predicted structure of *Pf*NRAMP (Figure 5) reflects the state that is open towards the cytosol as in the crystal structure of NRAMP from *Deinococcus radiodurans* (Bozzi et al., 2016). While a negatively charged cavity inside the protein is clearly visible in the *Pf*NRAMP model, the proposed outward-facing permeation pathway for metal ions is likely occluded in this conformation (Figure 5C). It is conceivable that Fe^{2+} ions permeate through this pathway from the DV lumen and bind to the charged cavity like the Mn^{2+} ion to *S. capitis* NRAMP/DMT (Supplementary Figure S4D). *Pf*NRAMP might function similarly to its ortholog in *D. radiodurans*, which was shown to mediate pH-dependent transport of Fe^{2+} and Mn^{2+} in symport with H^+ using uptake assays in *E. coli*, HEK293T cells, and proteoliposomes (Bozzi et al., 2016; Bozzi et al., 2019).

Expression of the surface protein *Pf*E140 was upregulated when iron levels were low compared to standard conditions ($\log_2$ FC = 0.65, P = 0.0006, Table 1) and the GFP fusion protein localized to the PPM only, as evidenced by the fluorescent edges of free merozoites (Figure 3D). This observation is consistent with the fact that the extracellular portions of this protein are highly polymorphic because of their exposure to the immune system at the sporozoite stage (Meerstein-Kessel et al., 2021). Interestingly, vaccines targeting *Py*E140 in *Plasmodium yoelii* were reported to induce up to 100% sterile protection mediated by antibodies in mice (Smith et al., 2020). The reduced parasite replication rate upon its conditional knockdown demonstrates the importance of *Pf*E140 for parasite growth and the rescue of the *Pf*E140 knockdown by hepcidin treatment support a role of this putative transporter in iron uptake (Figure 4F). Its predicted essential nature (Zhang et al., 2018), in addition to the absence of orthologs in humans, make it an excellent drug target candidate. While our *P. falciparum* gene expression data (Figures 2B, D) point towards a role of *Pf*E140 in iron homeostasis, its precise function is still unclear and it remains to be clarified whether the large coiled-coil domain exposed to the extracellular space (Figure 5) can mediate dimerization upon substrate binding. Given our experimental results and the functional annotations (Figure 5C; Supplementary Figure S5), we hypothesize that *Pf*E140 is a plasma membrane transporter for inorganic cations such as metal ions.

In conclusion, this is the first study to investigate *P. falciparum* transcriptomics under different iron conditions and to determine the subcellular localization of the known and putative iron transport proteins *Pf*MRS3, *Pf*VIT, *Pf*ZIPCO and *Pf*E140 as well as the growth effects of a *Pf*VIT or *Pf*ZIPCO knockout and an inducible *Pf*E140 knockdown. Our results reveal how the human malaria parasite reacts to alterations in host iron status and provide new insights into the mechanisms of iron transport in *P. falciparum* in addition to offering avenues for the development of novel therapeutic strategies against malaria. We propose a model for the regulation of iron homeostasis in the *P. falciparum*-infected erythrocyte with a series of six organelle-specific iron transport proteins in the parasite (Figure 6): One route of iron uptake into the parasite is through the release of Fe^{2+} upon hemoglobin digestion in the DV and the efflux of the ion into the cytosol mediated by *Pf*NRAMP (Loveridge and Sigala, 2024) and/or *Pf*CRT (Bakouh et al., 2017). Ferrous iron likely also enters the parasite cytosol across the PPM via *Pf*E140 and this pathway may be particularly important during schizogony, when the putative transporter gene is abundantly transcribed and new merozoites without a DV are formed (Broadbent et al., 2015). Once inside the cytosol, iron concentrations need to be tightly regulated to avoid toxicity, which could be achieved by Fe^{2+} import into the mitochondrion as the main site of iron utilization via *Pf*MRS3 and through transport into (*Pf*VIT) and out of (*Pf*ZIPCO) cytoplasmic vesicles functioning as labile iron pools. To confirm the hypotheses of our exploratory study, transport assays with purified proteins like those performed with recombinant *Pf*VIT (Labarbuta et al., 2017) are required for the formal demonstration of substrate specificities and activities of the other transporters in addition to further functional characterization of the proteins during the mosquito, liver and asexual blood stages of the parasite. As no ortholog of the essential *Pf*E140 and only a distant homolog of the non-redundant mitochondrial iron importer *Pf*MRS3 (Mather et al., 2007) are present in humans, these provide candidate targets for urgently needed new antimalarial drugs. Furthermore, dissecting how *P. falciparum* senses changes in micronutrient availability in its environment and how it modulates its virulence accordingly is an area of considerable interest for future investigation, as iron is an essential regulatory signal for virulence factors in many pathogens.

Data availability statement

The full RNA-sequencing datasets generated and analyzed in this study are available in the BioStudies repository (89) under accession number E-MTAB-13411: https://www.ebi.ac.uk/biostudies/studies/E-MTAB-13411. The code and data used for parasite age estimation can be accessed at Zenodo with the record ID 7996302: https://zenodo.org/record/7996302.

Ethics statement

Ethical approval was not required for the studies involving humans because the erythrocytes used in this study were residuals from voluntary blood donations at the University Medical Center Hamburg-Eppendorf. All donors provided written informed consent that their blood donation could be used for research

purposes. The studies were conducted in accordance with the local legislation and institutional requirements. The human samples used in this study were acquired from a by-product of routine care or industry. Written informed consent to participate in this study was not required from the participants or the participants' legal guardians/next of kin in accordance with the national legislation and the institutional requirements.

Author contributions

JW: Conceptualization, Data curation, Formal Analysis, Investigation, Methodology, Project administration, Software, Validation, Visualization, Writing – original draft, Writing – review & editing. VK: Formal Analysis, Software, Visualization, Writing – original draft, Writing – review & editing, Data curation, Investigation, Methodology, Validation. LV-N: Software, Visualization, Writing – review & editing, Formal Analysis. CN: Investigation, Writing – original draft. MG: Resources, Project administration, Writing – original draft. SPe: Project administration, Resources, Writing – original draft. SPo: Funding acquisition, Resources, Supervision, Writing – review & editing. JS: Conceptualization, Formal Analysis, Funding acquisition, Methodology, Project administration, Software, Visualization, Writing – original draft, Writing – review & editing, Data curation, Validation.

Funding

The author(s) declare that financial support was received for the research, authorship, and/or publication of this article. This work was supported by a Boehringer Ingelheim Foundation Exploration Grant, the Partnership for Innovation, Education and Research (PIER) of Hamburg University and DESY (project PIF-2018-87) and the European Molecular Biology Laboratory (EMBL). JW was additionally funded by the European Research Council (ERC) under the European Union's Horizon 2020 Research and Innovation Program (grant agreement 759534) and VK by a research fellowship from the EMBL Interdisciplinary Postdoc (EIPOD) Program under Marie Curie Cofund Actions MSCA-COFUND-FP (grant agreement 847543). The funders had no role in study design, data collection and analysis, decision to publish, or preparation of the manuscript.

Acknowledgments

The authors thank the Genomics Core Facility at EMBL Heidelberg, especially Vladimir Benes, for the RNA-sequencing service, and EMBL Hamburg for the provision of research and technical support as well as access to research infrastructures. Grzegorz Chojnowski and the group of Jan Kosinski at EMBL Hamburg enabled the AlphaFold2 workflow at the EMBL Hamburg computer cluster. The Advanced Light and Fluorescence Microscopy Facility at CSSB Hamburg, in particular Roland Thünauer, supported microscopy experiments and the Bernhard Nocht Institute for Tropical Medicine (BNITM) provided lab space. We gratefully acknowledge Tobias Spielmann for pSLI-GFP and pARL-*Pf*ACP (1–60)-mCherry, Paul Burda for pSLI-GFP-*glmS*, Jacobus Pharmaceuticals for WR99210, Anna Bachmann and Mayka Sánchez for helpful advice, Eileen Devaney, Katharina Jungnickel, and Samuel Pažický for critical reading of the manuscript, and Heidrun von Thien, Yannick Höppner, and Gabriela Guédez for technical assistance. A preprint of this article is available on bioRxiv at https://doi.org/10.1101/2024.04.18.590068 (Wunderlich et al., 2024).

Conflict of interest

The authors declare that the research was conducted in the absence of any commercial or financial relationships that could be construed as a potential conflict of interest.

Publisher's note

Supplementary material

The Supplementary Material for this article can be found online at: https://www.frontiersin.org/articles/10.3389/fcimb.2024.1480076/full#supplementary-material

References

Abrahamian, M., Ah-Fong, A. M., Davis, C., Andreeva, K., and Judelson, H. S. (2016). Gene expression and silencing studies in *Phytophthora infestans* reveal infection-specific nutrient transporters and a role for the nitrate reductase pathway in plant pathogenesis. *PloS Pathog.* 12, e1006097. doi: 10.1371/journal.ppat.1006097

Aghabi, D., Sloan, M., Gill, G., Hartmann, E., Antipova, O., Dou, Z., et al. (2023). The vacuolar iron transporter mediates iron detoxification in Toxoplasma gondii. *Nat. Commun.* 14, 3659. doi: 10.1038/s41467-023-39436-y

Agrawal, S., and Striepen, B. (2010). More membranes, more proteins: complex protein import mechanisms into secondary plastids. *Protist.* 161, 672–687. doi: 10.1016/j.protis.2010.09.002

Ahiya, A. I., Bhatnagar, S., Morrisey, J. M., Beck, J. R., and Vaidya, A. B. (2022). Dramatic consequences of reducing erythrocyte membrane cholesterol on *Plasmodium falciparum*. *Microbiol. Spectr.* 10, e0015822. doi: 10.1128/spectrum.00158-22

Altschul, S. F., Madden, T. L., Schäffer, A. A., Zhang, J., Zhang, Z., Miller, W., et al. (1997). Gapped BLAST and PSI-BLAST: a new generation of protein database search programs. *Nucleic Acids Res.* 25, 3389–3402. doi: 10.1093/nar/25.17.3389

Andrews, S. (2010). *FastQC: a quality control tool for high throughput sequence data* (Cambridge, UK: Babraham Bioinformatics, Babraham Institute).

Aschemeyer, S., Qiao, B., Stefanova, D., Valore, E. V., Sek, A. C., Ruwe, T. A., et al. (2018). Structure-function analysis of ferroportin defines the binding site and an alternative mechanism of action of hepcidin. *Blood.* 131, 899–910. doi: 10.1182/blood-2017-05-786590

Aurrecoechea, C., Brestelli, J., Brunk, B. P., Dommer, J., Fischer, S., Gajria, B., et al. (2009). PlasmoDB: a functional genomic database for malaria parasites. *Nucleic Acids Res.* 37, D539–DD43. doi: 10.1093/nar/gkn814

Bakouh, N., Bellanca, S., Nyboer, B., Moliner Cubel, S., Karim, Z., Sanchez, C. P., et al. (2017). Iron is a substrate of the Plasmodium falciparum chloroquine resistance transporter *Pf*CRT in Xenopus oocytes. *J. Biol. Chem.* 292, 16109–16121. doi: 10.1074/jbc.M117.805200

Becker, K., Tilley, L., Vennerstrom, J. L., Roberts, D., Rogerson, S., and Ginsburg, H. (2004). Oxidative stress in malaria parasite-infected erythrocytes: host–parasite interactions. *Int. J. Parasitol.* 34, 163–189. doi: 10.1016/j.ijpara.2003.09.011

Benjamini, Y., and Hochberg, Y. (1995). Controlling the false discovery rate: a practical and powerful approach to multiple Testing. *J. R. Stat. Soc. Ser. B.* 57, 289–300. doi: 10.1111/j.2517-6161.1995.tb02031.x

Billesbølle, C. B., Azumaya, C. M., Kretsch, R. C., Powers, A. S., Gonen, S., Schneider, S., et al. (2020). Structure of hepcidin-bound ferroportin reveals iron homeostatic mechanisms. *Nature*. 586, 807–811. doi: 10.1038/s41586-020-2668-z

Birnbaum, J., Flemming, S., Reichard, N., Soares, A. B., Mesén-Ramírez, P., Jonscher, E., et al. (2017). A genetic system to study Plasmodium falciparum protein function. *Nat. Methods* 14, 450–456. doi: 10.1038/nmeth.4223

Birnbaum, J., Scharf, S., Schmidt, S., Jonscher, E., Hoeijmakers, W. A. M., Flemming, S., et al. (2020). A Kelch13-defined endocytosis pathway mediates artemisinin resistance in malaria parasites. *Science.* 367, 51–59. doi: 10.1126/science.aax4735

Blighe, K., Rana, S., and Lewis, M. (2022). EnhancedVolcano: Publication-ready volcano plots with enhanced colouring and labeling. *R Package version.* 1, 15. doi: 10.18129/B9.bioc.EnhancedVolcano

Blume, M., Hliscs, M., Rodriguez-Contreras, D., Sanchez, M., Landfear, S., Lucius, R., et al. (2011). A constitutive pan-hexose permease for the *Plasmodium* life cycle and transgenic models for screening of antimalarial sugar analogs. *FASEB J.* 25, 1218–1229. doi: 10.1096/fj.10-173278

Boucher, M. J., Ghosh, S., Zhang, L., Lal, A., Jang, S. W., Ju, A., et al. (2018). Integrative proteomics and bioinformatic prediction enable a high-confidence apicoplast proteome in malaria parasites. *PloS Biol.* 16, e2005895. doi: 10.1371/journal.pbio.2005895

Bozdech, Z., Llinás, M., Pulliam, B. L., Wong, E. D., Zhu, J., and DeRisi, J. L. (2003). The transcriptome of the intraerythrocytic developmental cycle of *Plasmodium falciparum*. *PloS Biol.* 1, E5. doi: 10.1371/journal.pbio.0000005

Bozzi, A. T., Bane, L. B., Weihofen, W. A., Singharoy, A., Guillen, E. R., Ploegh, H. L., et al. (2016). Crystal structure and conformational change mechanism of a bacterial Nramp-family divalent metal transporter. *Structure.* 24, 2102–2114. doi: 10.1016/j.str.2016.09.017

Bozzi, A. T., Bane, L. B., Zimanyi, C. M., and Gaudet, R. (2019). Unique structural features in an Nramp metal transporter impart substrate-specific proton cotransport and a kinetic bias to favor import. *J. Gen. Physiol.* 151, 1413–1429. doi: 10.1085/jgp.201912428

Brabin, L., Roberts, S. A., Tinto, H., Gies, S., Diallo, S., and Brabin, B. (2020). Iron status of Burkinabé adolescent girls predicts malaria risk in the following rainy season. *Nutrients.* 12 (5), 1446. doi: 10.3390/nu12051446

Brancucci, N. M. B., Gerdt, J. P., Wang, C., De Niz, M., Philip, N., Adapa, S. R., et al. (2017). Lysophosphatidylcholine regulates sexual stage differentiation in the human malaria parasite *Plasmodium falciparum*. *Cell* 171, 1532–44.e15. doi: 10.1016/j.cell.2017.10.020

Brazzolotto, X., Pierrel, F., and Pelosi, L. (2014). Three conserved histidine residues contribute to mitochondrial iron transport through mitoferrins. *Biochem. J.* 460, 79–89. doi: 10.1042/BJ20140107

Broadbent, K. M., Broadbent, J. C., Ribacke, U., Wirth, D., Rinn, J. L., and Sabeti, P. C. (2015). Strand-specific RNA sequencing in Plasmodium falciparum malaria identifies developmentally regulated long non-coding RNA and circular RNA. *BMC Genomics* 16, 454. doi: 10.1186/s12864-015-1603-4

Brown, R. A. M., Richardson, K. L., Kabir, T. D., Trinder, D., Ganss, R., and Leedman, P. J. (2020). Altered iron metabolism and impact in cancer biology, metastasis, and immunology. *Front. Oncol.* 10, 476. doi: 10.3389/fonc.2020.00476

Burda, P. C., Crosskey, T., Lauk, K., Zurborg, A., Söhnchen, C., Liffner, B., et al. (2020). Structure-based identification and functional characterization of a lipocalin in the malaria parasite *Plasmodium falciparum*. *Cell Rep.* 31, 107817. doi: 10.1016/j.celrep.2020.107817

Bushell, E., Gomes, A. R., Sanderson, T., Anar, B., Girling, G., Herd, C., et al. (2017). Functional profiling of a *Plasmodium* genome reveals an abundance of essential genes. *Cell.* 170, 260–72.e8. doi: 10.1016/j.cell.2017.06.030

Carter, N. S., Ben Mamoun, C., Liu, W., Silva, E. O., Landfear, S. M., Goldberg, D. E., et al. (2000). Isolation and functional characterization of the *Pf*NT1 nucleoside transporter gene from *Plasmodium falciparum*. *J. Biol. Chem.* 275, 10683–10691. doi: 10.1074/jbc.275.14.10683

Cercamondi, C. I., Egli, I. M., Ahouandjinou, E., Dossa, R., Zeder, C., Salami, L., et al. (2010). Afebrile Plasmodium falciparum parasitemia decreases absorption of fortification iron but does not affect systemic iron utilization: a double stable-isotope study in young Beninese women. *Am. J. Clin. Nutr.* 92, 1385–1392. doi: 10.3945/ajcn.2010.30051

Chitale, M., Hawkins, T., Park, C., and Kihara, D. (2009). ESG: extended similarity group method for automated protein function prediction. *Bioinformatics.* 25, 1739–1745. doi: 10.1093/bioinformatics/btp309

Chou, E. S., Abidi, S. Z., Teye, M., Leliwa-Sytek, A., Rask, T. S., Cobbold, S. A., et al. (2018). A high parasite density environment induces transcriptional changes and cell death in Plasmodium falciparum blood stages. *FEBS J.* 285, 848–870. doi: 10.1111/febs.2018.285.issue-5

Clark, M. A., Goheen, M. M., Fulford, A., Prentice, A. M., Elnagheeb, M. A., Patel, J., et al. (2014). Host iron status and iron supplementation mediate susceptibility to erythrocytic stage *Plasmodium falciparum*. *Nat. Commun.* 5, 4446. doi: 10.1038/ncomms5446

Cowell, A. N., Istvan, E. S., Lukens, A. K., Gomez-Lorenzo, M. G., Vanaerschot, M., Sakata-Kato, T., et al. (2018). Mapping the malaria parasite druggable genome by using in *vitro* evolution and chemogenomics. *Science.* 359, 191–199. doi: 10.1126/science.aan4472

Crameri, F., Shephard, G. E., and Heron, P. J. (2020). The misuse of color in science communication. *Nat. Commun.* 11, 5444. doi: 10.1038/s41467-020-19160-7

de Oliveira, L. S., Alborghetti, M. R., Carneiro, R. G., Bastos, I. M. D., Amino, R., Grellier, P., et al. (2021). Calcium in the backstage of malaria parasite biology. *Front. Cell Infect. Microbiol.* 11, 708834. doi: 10.3389/fcimb.2021.708834

Dobin, A., Davis, C. A., Schlesinger, F., Drenkow, J., Zaleski, C., Jha, S., et al. (2013). STAR: ultrafast universal RNA-seq aligner. *Bioinformatics.* 29, 15–21. doi: 10.1093/bioinformatics/bts635

Drakesmith, H., and Prentice, A. (2008). Viral infection and iron metabolism. *Nat. Rev. Microbiol.* 6, 541–552. doi: 10.1038/nrmicro1930

Duraisingh, M. T., and Skillman, K. M. (2018). Epigenetic variation and regulation in malaria parasites. *Annu. Rev. Microbiol.* 72, 355–375. doi: 10.1146/annurev-micro-090817-062722

Ecker, A., Lakshmanan, V., Sinnis, P., Coppens, I., and Fidock, D. A. (2011). Evidence that mutant *Pf*CRT facilitates the transmission to mosquitoes of chloroquine-treated *Plasmodium* gametocytes. *J. Infect. Dis.* 203, 228–236. doi: 10.1093/infdis/jiq036

Edayé, S., and Georges, E. (2015). Characterization of native PfABCG protein in *Plasmodium falciparum*. *Biochem. Pharmacol.* 97, 137–146. doi: 10.1016/j.bcp.2015.06.035

Egan, T. J., Combrinck, J. M., Egan, J., Hearne, G. R., Marques, H. M., Ntenteni, S., et al. (2002). Fate of haem iron in the malaria parasite *Plasmodium falciparum*. *Biochem. J.* 365, 343–347. doi: 10.1042/bj20020793

Ehrnstorfer, I. A., Geertsma, E. R., Pardon, E., Steyaert, J., and Dutzler, R. (2014). Crystal structure of a SLC11 (NRAMP) transporter reveals the basis for transition-metal ion transport. *Nat. Struct. Mol. Biol.* 21, 990–996. doi: 10.1038/nsmb.2904

Evans, R., O'Neill, M., Pritzel, A., Antropova, N., Senior, A., Green, T., et al. (2022). Protein complex prediction with AlphaFold-Multimer. *bioRxiv*. doi: 10.1101/2021.10.04.463034

Ewels, P., Magnusson, M., Lundin, S., and Käller, M. (2016). MultiQC: summarize analysis results for multiple tools and samples in a single report. *Bioinformatics.* 32, 3047–3048. doi: 10.1093/bioinformatics/btw354

Friedrich, O., Reiling, S. J., Wunderlich, J., and Rohrbach, P. (2014). Assessment of Plasmodium falciparum PfMDR1 transport rates using Fluo-4. *J. Cell Mol. Med.* 18, 1851–1862. doi: 10.1111/jcmm.2014.18.issue-9

Froschauer, E. M., Schweyen, R. J., and Wiesenberger, G. (2009). The yeast mitochondrial carrier proteins Mrs3p/Mrs4p mediate iron transport across the inner mitochondrial membrane. *Biochim. Biophys. Acta* 1788, 1044–1050. doi: 10.1016/j.bbamem.2009.03.004

Gardner, M. J., Hall, N., Fung, E., White, O., Berriman, M., Hyman, R. W., et al. (2002). Genome sequence of the human malaria parasite *Plasmodium falciparum*. *Nature* 419, 498–511. doi: 10.1038/nature01097

Ginzburg, Y. Z. (2019). Hepcidin-ferroportin axis in health and disease. *Vitam Horm.* 110, 17–45. doi: 10.1016/bs.vh.2019.01.002

Gligorijević, V., Renfrew, P. D., Kosciolek, T., Leman, J. K., Berenberg, D., Vatanen, T., et al. (2021). Structure-based protein function prediction using graph convolutional networks. *Nat. Commun.* 12, 3168. doi: 10.1038/s41467-021-23303-9

Goddard, T. D., Huang, C. C., Meng, E. C., Pettersen, E. F., Couch, G. S., Morris, J. H., et al. (2018). UCSF ChimeraX: Meeting modern challenges in visualization and analysis. *Protein Sci.* 27, 14–25. doi: 10.1002/pro.v27.1

Goheen, M. M., Bah, A., Wegmüller, R., Verhoef, H., Darboe, B., Danso, E., et al. (2017). Host iron status and erythropoietic response to iron supplementation determines susceptibility to the RBC stage of falciparum malaria during pregnancy. *Sci. Rep.* 7, 17674. doi: 10.1038/s41598-017-16896-z

Gupta, Y., Sharma, N., Singh, S., Romero, J. G., Rajendran, V., Mogire, R. M., et al. (2022). The multistage antimalarial compound calxinin perturbates P. falciparum Ca^{2+} homeostasis by targeting a unique ion channel. *Pharmaceutics.* 14, 1371. doi: 10.3390/pharmaceutics14071371

Gwamaka, M., Kurtis, J. D., Sorensen, B. E., Holte, S., Morrison, R., Mutabingwa, T. K., et al. (2012). Iron deficiency protects against severe Plasmodium falciparum malaria and death in young children. *Clin. Infect. Dis.* 54, 1137–1144. doi: 10.1093/cid/cis010

Hayashi, M., Yamada, H., Mitamura, T., Horii, T., Yamamoto, A., and Moriyama, Y. (2000). Vacuolar H^+-ATPase localized in plasma membranes of malaria parasite cells, Plasmodium falciparum, is involved in regional acidification of parasitized erythrocytes. *J. Biol. Chem.* 275, 34353–34358. doi: 10.1074/jbc.M003323200

Hodges, M., Yikilmaz, E., Patterson, G., Kasvosve, I., Rouault, T. A., Gordeuk, V. R., et al. (2005). An iron regulatory-like protein expressed in Plasmodium falciparum displays aconitase activity. *Mol. Biochem. Parasitol.* 143, 29–38. doi: 10.1016/j.molbiopara.2005.05.004

Huang, G., Ulrich, P. N., Storey, M., Johnson, D., Tischer, J., Tovar, J. A., et al. (2014). Proteomic analysis of the acidocalcisome, an organelle conserved from bacteria to human cells. *PloS Pathog.* 10, e1004555. doi: 10.1371/journal.ppat.1004555

Jonker, J. W., Buitelaar, M., Wagenaar, E., van der Valk, M. A., Scheffer, G. L., Scheper, R. J., et al. (2002). The breast cancer resistance protein protects against a major chlorophyll-derived dietary phototoxin and protoporphyria. *Proc. Natl. Acad. Sci. U S A.* 99, 15649–15654. doi: 10.1073/pnas.202607599

Jumper, J., Evans, R., Pritzel, A., Green, T., Figurnov, M., Ronneberger, O., et al. (2021). Highly accurate protein structure prediction with AlphaFold. *Nature.* 596, 583–589. doi: 10.1038/s41586-021-03819-2

Kang, D., and Kirienko, N. V. (2018). Interdependence between iron acquisition and biofilm formation in Pseudomonas aeruginosa. *J. Microbiol.* 56, 449–457. doi: 10.1007/s12275-018-8114-3

Kato, T., Kumazaki, K., Wada, M., Taniguchi, R., Nakane, T., Yamashita, K., et al. (2019). Crystal structure of plant vacuolar iron transporter VIT1. *Nat. Plants.* 5, 308–315. doi: 10.1038/s41477-019-0367-2

Kenthirapalan, S., Waters, A. P., Matuschewski, K., and Kooij, T. W. (2014). Copper-transporting ATPase is important for malaria parasite fertility. *Mol. Microbiol.* 91, 315–325. doi: 10.1111/mmi.2014.91.issue-2

Kidgell, C., Volkman, S. K., Daily, J., Borevitz, J. O., Plouffe, D., Zhou, Y., et al. (2006). A systematic map of genetic variation in *Plasmodium falciparum*. *PloS Pathog.* 2, e57. doi: 10.1371/journal.ppat.0020057

Kim, C. H., Kim, H. K., Bae, S. J., Park, J. Y., and Lee, K. U. (2011). Association of elevated serum ferritin concentration with insulin resistance and impaired glucose metabolism in Korean men and women. *Metabolism.* 60, 414–420. doi: 10.1016/j.metabol.2010.03.007

Kim, J., Tan, Y. Z., Wicht, K. J., Erramilli, S. K., Dhingra, S. K., Okombo, J., et al. (2019). Structure and drug resistance of the *Plasmodium falciparum* transporter PfCRT. *Nature*. 576, 315–320. doi: 10.1038/s41586-019-1795-x

Kloehn, J., Harding, C. R., and Soldati-Favre, D. (2021). Supply and demand - heme synthesis, salvage and utilization by Apicomplexa. *FEBS J.* 288 (2), 382–404. doi: 10.1111/febs.15445

Knovich, M. A., Storey, J. A., Coffman, L. G., Torti, S. V., and Torti, F. M. (2009). Ferritin for the clinician. *Blood Rev.* 23, 95–104. doi: 10.1016/j.blre.2008.08.001

Kuhn, Y., Sanchez, C. P., Ayoub, D., Saridaki, T., Van Dorsselaer, A., and Lanzer, M. (2010). Trafficking of the phosphoprotein PfCRT to the digestive vacuolar membrane in *Plasmodium falciparum*. *Traffic* 11, 236–249. doi: 10.1111/j.1600-0854.2009.01018.x

Küpper, H., and Kochian, L. V. (2010). Transcriptional regulation of metal transport genes and mineral nutrition during acclimatization to cadmium and zinc in the Cd/Zn hyperaccumulator, *Thlaspi caerulescens* (Ganges population). *New Phytol.* 185, 114–129. doi: 10.1111/j.1469-8137.2009.03051.x

Labarbuta, P., Duckett, K., Botting, C. H., Chahrour, O., Malone, J., Dalton, J. P., et al. (2017). Recombinant vacuolar iron transporter family homologue *Pf*VIT from human malaria-causing Plasmodium falciparum is a Fe^{2+}/H^+exchanger. *Sci. Rep.* 7, 42850. doi: 10.1038/srep42850

Lambros, C., and Vanderberg, J. P. (1979). Synchronization of Plasmodium falciparum erythrocytic stages in culture. *J. Parasitol.* 65, 418–420. doi: 10.2307/3280287

Lee, H. J., Georgiadou, A., Walther, M., Nwakanma, D., Stewart, L. B., Levin, M., et al. (2018). Integrated pathogen load and dual transcriptome analysis of systemic host-pathogen interactions in severe malaria. *Sci. Transl. Med.* 10 (447), eaar3619. doi: 10.1126/scitranslmed.aar3619

Lemieux, J. E., Gomez-Escobar, N., Feller, A., Carret, C., Amambua-Ngwa, A., Pinches, R., et al. (2009). Statistical estimation of cell-cycle progression and lineage commitment in Plasmodium falciparum reveals a homogeneous pattern of transcription in *ex vivo* culture. *Proc. Natl. Acad. Sci. U S A.* 106, 7559–7564. doi: 10.1073/pnas.0811829106

Lerch, A., Koepfli, C., Hofmann, N. E., Messerli, C., Wilcox, S., Kattenberg, J. H., et al. (2017). Development of amplicon deep sequencing markers and data analysis pipeline for genotyping multi-clonal malaria infections. *BMC Genomics* 18, 864. doi: 10.1186/s12864-017-4260-y

Li, H., Handsaker, B., Wysoker, A., Fennell, T., Ruan, J., Homer, N., et al. (2009). The sequence alignment/map format and SAMtools. *Bioinformatics.* 25, 2078–2079. doi: 10.1093/bioinformatics/btp352

Li, L., Murdock, G., Bagley, D., Jia, X., Ward, D. M., and Kaplan, J. (2010). Genetic dissection of a mitochondria-vacuole signaling pathway in yeast reveals a link between chronic oxidative stress and vacuolar iron transport. *J. Biol. Chem.* 285, 10232–10242. doi: 10.1074/jbc.M109.096859

Liao, Y., Smyth, G. K., and Shi, W. (2013). The Subread aligner: fast, accurate and scalable read mapping by seed-and-vote. *Nucleic Acids Res.* 41, e108. doi: 10.1093/nar/gkt214

Liao, Y., Smyth, G. K., and Shi, W. (2014). featureCounts: an efficient general purpose program for assigning sequence reads to genomic features. *Bioinformatics.* 30, 923–930. doi: 10.1093/bioinformatics/btt656

Lim, L., Linka, M., Mullin, K. A., Weber, A. P., and McFadden, G. I. (2010). The carbon and energy sources of the non-photosynthetic plastid in the malaria parasite. *FEBS Lett.* 584, 549–554. doi: 10.1016/j.febslet.2009.11.097

Loveridge, K. M., and Sigala, P. A. (2024). Unraveling mechanisms of iron acquisition in malaria parasites. *bioRxiv*. doi: 10.1101/2024.05.10.587216

Loyevsky, M., John, C., Dickens, B., Hu, V., Miller, J. H., and Gordeuk, V. R. (1999). Chelation of iron within the erythrocytic *Plasmodium falciparum* parasite by iron chelators. *Mol. Biochem. Parasitol.* 101, 43–59. doi: 10.1016/S0166-6851(99)00053-5

Loyevsky, M., LaVaute, T., Allerson, C. R., Stearman, R., Kassim, O. O., Cooperman, S., et al. (2001). An IRP-like protein from Plasmodium falciparum binds to a mammalian iron-responsive element. *Blood*. 98, 2555–2562. doi: 10.1182/blood.V98.8.2555

Mach, J., and Sutak, R. (2020). Iron in parasitic protists – from uptake to storage and where we can interfere. *Metallomics.* 12, 1335–1347. doi: 10.1039/d0mt00125b

Magowan, C., Brown, J. T., Liang, J., Heck, J., Coppel, R. L., Mohandas, N., et al. (1997). Intracellular structures of normal and aberrant Plasmodium falciparum malaria parasites imaged by soft x-ray microscopy. *Proc. Natl. Acad. Sci. U S A.* 94, 6222–6227. doi: 10.1073/pnas.94.12.6222

Malleret, B., Claser, C., Ong, A. S., Suwanarusk, R., Sriprawat, K., Howland, S. W., et al. (2011). A rapid and robust tri-color flow cytometry assay for monitoring malaria parasite development. *Sci. Rep.* 1, 118. doi: 10.1038/srep00118

Mancio-Silva, L., Slavic, K., Grilo Ruivo, M. T., Grosso, A. R., Modrzynska, K. K., Vera, I. M., et al. (2017). Nutrient sensing modulates malaria parasite virulence. *Nature.* 547, 213–216. doi: 10.1038/nature23009

Marapana, D. S., Dagley, L. F., Sandow, J. J., Nebl, T., Triglia, T., Pasternak, M., et al. (2018). Plasmepsin V cleaves malaria effector proteins in a distinct endoplasmic reticulum translocation interactome for export to the erythrocyte. *Nat. Microbiol.* 3, 1010–1022. doi: 10.1038/s41564-018-0219-2

Marfil-Rivera, L. J. (2015). Iron overload. *Medicina Universitaria.* 17, 240–242. doi: 10.1016/j.rmu.2015.08.001

Martin, M. (2011). Cutadapt removes adapter sequences from high-throughput sequencing reads. *EMBnet J.* 17, 10–12. doi: 10.14806/ej.17.1.200

Martin, R. E. (2020). The transportome of the malaria parasite. *Biol. Rev. Camb Philos. Soc* 95, 305–332. doi: 10.1111/brv.12565

Martin, R. E., Henry, R. I., Abbey, J. L., Clements, J. D., and Kirk, K. (2005). The 'permeome' of the malaria parasite: an overview of the membrane transport proteins of *Plasmodium falciparum*. *Genome Biol.* 6, R26. doi: 10.1186/gb-2005-6-3-r26

Mather, M. W., Henry, K. W., and Vaidya, A. B. (2007). Mitochondrial drug targets in apicomplexan parasites. *Curr. Drug Targets.* 8, 49–60. doi: 10.2174/138945007779315632

Mathew, R., Wunderlich, J., Thivierge, K., Cwiklinski, K., Dumont, C., Tilley, L., et al. (2021). Biochemical and cellular characterization of the Plasmodium falciparum M1 alanyl aminopeptidase (*Pf*M1AAP) and M17 leucyl aminopeptidase (*Pf*M17LAP). *Sci. Rep.* 11, 2854. doi: 10.1038/s41598-021-82499-4

Meerstein-Kessel, L., Venhuizen, J., Garza, D., Proellochs, N. I., Vos, E. J., Obiero, J. M., et al. (2021). Novel insights from the Plasmodium falciparum sporozoite-specific proteome by probabilistic integration of 26 studies. *PloS Comput. Biol.* 17, e1008067. doi: 10.1371/journal.pcbi.1008067

Meng, E. C., Pettersen, E. F., Couch, G. S., Huang, C. C., and Ferrin, T. E. (2006). Tools for integrated sequence-structure analysis with UCSF Chimera. *BMC Bioinf.* 7, 339. doi: 10.1186/1471-2105-7-339

Mesén-Ramírez, P., Bergmann, B., Elhabiri, M., Zhu, L., von Thien, H., Castro-Peña, C., et al. (2021). The parasitophorous vacuole nutrient channel is critical for drug access in malaria parasites and modulates the artemisinin resistance fitness cost. *Cell Host Microbe*. 29 (12), 1774–1787.e9. doi: 10.1016/j.chom.2021.11.002

Milner, D. A. Jr., Pochet, N., Krupka, M., Williams, C., Seydel, K., Taylor, T. E., et al. (2012). Transcriptional profiling of Plasmodium falciparum parasites from patients with severe malaria identifies distinct low vs. high parasitemic clusters. *PloS One* 7, e40739. doi: 10.1371/journal.pone.0040739

Moon, R. W., Hall, J., Rangkuti, F., Ho, Y. S., Almond, N., Mitchell, G. H., et al. (2013). Adaptation of the genetically tractable malaria pathogen *Plasmodium knowlesi* to continuous culture in human erythrocytes. *Proc. Natl. Acad. Sci. U S A.* 110, 531–536. doi: 10.1073/pnas.1216457110

Moonah, S., Sanders, N. G., Persichetti, J. K., and Sullivan, D. J. Jr. (2014). Erythrocyte lysis and *Xenopus laevis* oocyte rupture by recombinant Plasmodium falciparum hemolysin III. *Eukaryot Cell.* 13, 1337–1345. doi: 10.1128/EC.00088-14

Muckenthaler, M. U., Rivella, S., Hentze, M. W., and Galy, B. (2017). A red carpet for iron metabolism. *Cell.* 168, 344–361. doi: 10.1016/j.cell.2016.12.034

Mühlenhoff, U., Stadler, J. A., Richhardt, N., Seubert, A., Eickhorst, T., Schweyen, R. J., et al. (2003). A specific role of the yeast mitochondrial carriers Mrs3/4p in mitochondrial iron acquisition under iron-limiting conditions. *J. Biol. Chem.* 278, 40612–40620. doi: 10.1074/jbc.M307847200

Muriuki, J. M., Mentzer, A. J., Mitchell, R., Webb, E. L., Etyang, A. O., Kyobutungi, C., et al. (2021). Malaria is a cause of iron deficiency in African children. *Nat. Med.* 27, 653–658. doi: 10.1038/s41591-021-01238-4

Newhouse, I. J., Clement, D. B., and Lai, C. (1993). Effects of iron supplementation and discontinuation on serum copper, zinc, calcium, and magnesium levels in women. *Med. Sci. Sports Exerc.* 25, 562–571. doi: 10.1249/00005768-199305000-00006

Nozawa, A., Ito, D., Ibrahim, M., Santos, H. J., Tsuboi, T., and Tozawa, Y. (2020). Characterization of mitochondrial carrier proteins of malaria parasite Plasmodium falciparum based on in *vitro* translation and reconstitution. *Parasitol. Int.* 79, 102160. doi: 10.1016/j.parint.2020.102160

Nyakeriga, A. M., Troye-Blomberg, M., Dorfman, J. R., Alexander, N. D., Bäck, R., Kortok, M., et al. (2004). Iron deficiency and malaria among children living on the coast of Kenya. *J. Infect. Dis.* 190, 439–447. doi: 10.1086/jid.2004.190.issue-3

Paganini, D., and Zimmermann, M. B. (2017). The effects of iron fortification and supplementation on the gut microbiome and diarrhea in infants and children: a review. *Am. J. Clin. Nutr.* 106, 1688s–1693s. doi: 10.3945/ajcn.117.156067

Pang, C., Chai, J., Zhu, P., Shanklin, J., and Liu, Q. (2023). Structural mechanism of intracellular autoregulation of zinc uptake in ZIP transporters. *Nat. Commun.* 14, 3404. doi: 10.1038/s41467-023-39010-6

Park, D. J., Lukens, A. K., Neafsey, D. E., Schaffner, S. F., Chang, H. H., Valim, C., et al. (2012). Sequence-based association and selection scans identify drug resistance loci in the Plasmodium falciparum malaria parasite. *Proc. Natl. Acad. Sci. U S A.* 109, 13052–13067. doi: 10.1073/pnas.1210585109

Petrat, F., Rauen, U., and de Groot, H. (1999). Determination of the chelatable iron pool of isolated rat hepatocytes by digital fluorescence microscopy using the fluorescent probe, phen green SK. *Hepatology.* 29, 1171–1179. doi: 10.1002/hep.510290435

Prommana, P., Uthaipibull, C., Wongsombat, C., Kamchonwongpaisan, S., Yuthavong, Y., Knuepfer, E., et al. (2013). Inducible knockdown of *Plasmodium* gene expression using the *glmS* ribozyme. *PloS One* 8, e73783. doi: 10.1371/journal.pone.0073783

Raudvere, U., Kolberg, L., Kuzmin, I., Arak, T., Adler, P., Peterson, H., et al. (2019). g:Profiler: a web server for functional enrichment analysis and conversions of gene lists (2019 update). *Nucleic Acids Res.* 47, W191–W1W8. doi: 10.1093/nar/gkz369

Rivadeneira, E. M., Wasserman, M., and Espinal, C. T. (1983). Separation and concentration of schizonts of Plasmodium falciparum by Percoll gradients. *J. Protozool.* 30, 367–370. doi: 10.1111/j.1550-7408.1983.tb02932.x

Robinson, M. D., McCarthy, D. J., and Smyth, G. K. (2010). edgeR: a Bioconductor package for differential expression analysis of digital gene expression data. *Bioinformatics.* 26, 139–140. doi: 10.1093/bioinformatics/btp616

Rohrbach, P., Friedrich, O., Hentschel, J., Plattner, H., Fink, R. H., and Lanzer, M. (2005). Quantitative calcium measurements in subcellular compartments of Plasmodium falciparum-infected erythrocytes. *J. Biol. Chem.* 280, 27960–27969. doi: 10.1074/jbc.M500777200

Ruiz, F. A., Luo, S., Moreno, S. N., and Docampo, R. (2004). Polyphosphate content and fine structure of acidocalcisomes of *Plasmodium falciparum*. *Microsc Microanal* 10, 563–567. doi: 10.1017/S1431927604040875

Sahu, T., Boisson, B., Lacroix, C., Bischoff, E., Richier, Q., Formaglio, P., et al. (2014). ZIPCO, a putative metal ion transporter, is crucial for *Plasmodium* liver-stage development. *EMBO Mol. Med.* 6, 1387–1397. doi: 10.15252/emmm.201403868

Saier, M. H.Jr., Reddy, V. S., Tsu, B. V., Ahmed, M. S., Li, C., and Moreno-Hagelsieb, G. (2016). The Transporter Classification Database (TCDB): recent advances. *Nucleic Acids Res.* 44, D372–D3D9. doi: 10.1093/nar/gkv1103

Sanderson, T., and Rayner, J. C. (2017). PhenoPlasm: a database of disruption phenotypes for malaria parasite genes. *Wellcome Open Res.* 2, 45. doi: 10.12688/wellcomeopenres

Sarkans, U., Gostev, M., Athar, A., Behrangi, E., Melnichuk, O., Ali, A., et al. (2018). The BioStudies database - one stop shop for all data supporting a life sciences study. *Nucleic Acids Res.* 46, D1266–D1D70. doi: 10.1093/nar/gkx965

Sassmannshausen, J., Pradel, G., and Bennink, S. (2020). Perforin-like proteins of apicomplexan parasites. *Front. Cell Infect. Microbiol.* 10, 578883. doi: 10.3389/fcimb.2020.578883

Sayers, C. P., Mollard, V., Buchanan, H. D., McFadden, G. I., and Goodman, C. D. (2018). A genetic screen in rodent malaria parasites identifies five new apicoplast putative membrane transporters, one of which is essential in human malaria parasites. *Cell Microbiol.* 20, e12789. doi: 10.1111/cmi.12789

Schembri, L., Dalibart, R., Tomasello, F., Legembre, P., Ichas, F., and De Giorgi, F. (2007). The HA tag is cleaved and loses immunoreactivity during apoptosis. *Nat. Methods* 4, 107–108. doi: 10.1038/nmeth0207-107

Schindelin, J., Arganda-Carreras, I., Frise, E., Kaynig, V., Longair, M., Pietzsch, T., et al. (2012). Fiji: an open-source platform for biological-image analysis. *Nat. Methods* 9, 676–682. doi: 10.1038/nmeth.2019

Schmidt, O., Pfanner, N., and Meisinger, C. (2010). Mitochondrial protein import: from proteomics to functional mechanisms. *Nat. Rev. Mol. Cell Biol.* 11, 655–667. doi: 10.1038/nrm2959

Schnell, U., Dijk, F., Sjollema, K. A., and Giepmans, B. N. (2012). Immunolabeling artifacts and the need for live-cell imaging. *Nat. Methods* 9, 152–158. doi: 10.1038/nmeth.1855

Scholl, P. F., Tripathi, A. K., and Sullivan, D. J. (2005). Bioavailable iron and heme metabolism in *Plasmodium falciparum*. *Curr. Top. Microbiol. Immunol.* 295, 293–324. doi: 10.1007/3-540-29088-5_12

Schureck, M. A., Darling, J. E., Merk, A., Shao, J., Daggupati, G., Srinivasan, P., et al. (2021). Malaria parasites use a soluble RhopH complex for erythrocyte invasion and an integral form for nutrient uptake. *eLife.* 10, e65282. doi: 10.7554/eLife.65282

Sharma, P., Tóth, V., Hyland, E. M., and Law, C. J. (2021). Characterization of the substrate binding site of an iron detoxifying membrane transporter from *Plasmodium falciparum*. *Malar J.* 20, 295. doi: 10.1186/s12936-021-03827-7

Sheiner, L., and Soldati-Favre, D. (2008). Protein trafficking inside Toxoplasma gondii. *Traffic* 9, 636–646. doi: 10.1111/j.1600-0854.2008.00713.x

Shrivastava, D., Jha, A., Kabrambam, R., Vishwakarma, J., Mitra, K., Ramachandran, R., et al. (2024). Plasmodium falciparum ZIP1 is a zinc-selective transporter with stage-dependent targeting to the apicoplast and plasma membrane in erythrocytic parasites. *ACS Infect. Dis.* 10, 155–169. doi: 10.1021/acsinfecdis.3c00426

Sidik, S. M., Huet, D., Ganesan, S. M., Huynh, M. H., Wang, T., Nasamu, A. S., et al. (2016). A genome-wide CRISPR screen in *Toxoplasma* identifies essential apicomplexan genes. *Cell.* 166, 1423–35.e12. doi: 10.1016/j.cell.2016.08.019

Sigala, P. A., and Goldberg, D. E. (2014). The peculiarities and paradoxes of *Plasmodium* heme metabolism. *Annu. Rev. Microbiol.* 68, 259–278. doi: 10.1146/annurev-micro-091313-103537

Slavic, K., Krishna, S., Lahree, A., Bouyer, G., Hanson, K. K., Vera, I., et al. (2016). A vacuolar iron-transporter homologue acts as a detoxifier in Plasmodium. *Nat. Commun.* 7, 10403. doi: 10.1038/ncomms10403

Sloan, M. A., Aghabi, D., and Harding, C. R. (2021). Orchestrating a heist: uptake and storage of metals by apicomplexan parasites. *Microbiol. (Reading).* 167, 001114. doi: 10.1099/mic.0.001114

Smith, E. C., Limbach, K. J., Rangel, N., Oda, K., Bolton, J. S., Du, M., et al. (2020). Novel malaria antigen *Plasmodium yoelii* E140 induces antibody-mediated sterile protection in mice against malaria challenge. *PloS One* 15, e0232234. doi: 10.1371/journal.pone.0232234

Sousa Gerós, A., Simmons, A., Drakesmith, H., Aulicino, A., and Frost, J. N. (2020). The battle for iron in enteric infections. *Immunology.* 161, 186–199. doi: 10.1111/imm.v161.3

Spillman Natalie, J., Allen Richard, J. W., McNamara Case, W., Yeung Bryan, K. S., Winzeler Elizabeth, A., Diagana Thierry, T., et al. (2013). Na^+ regulation in the malaria parasite Plasmodium falciparum involves the cation ATPase *Pf*ATP4 and is a target of the spiroindolone antimalarials. *Cell Host Microbe* 13, 227–237. doi: 10.1016/j.chom.2012.12.006

Spork, S., Hiss, J. A., Mandel, K., Sommer, M., Kooij, T. W., Chu, T., et al. (2009). An unusual ERAD-like complex is targeted to the apicoplast of *Plasmodium falciparum*. *Eukaryot Cell* 8, 1134–1145. doi: 10.1128/EC.00083-09

Stanway, R. R., Bushell, E., Chiappino-Pepe, A., Roques, M., Sanderson, T., Franke-Fayard, B., et al. (2019). Genome-scale identification of essential metabolic processes for targeting the *Plasmodium* liver stage. *Cell.* 179, 1112–28.e26. doi: 10.1016/j.cell.2019.10.030

Stewart, L. B., Diaz-Ingelmo, O., Claessens, A., Abugri, J., Pearson, R. D., Goncalves, S., et al. (2020). Intrinsic multiplication rate variation and plasticity of human blood stage malaria parasites. *Commun. Biol.* 3, 624. doi: 10.1038/s42003-020-01349-7

Supek, F., Bošnjak, M., Škunca, N., and Šmuc, T. (2011). REVIGO summarizes and visualizes long lists of gene ontology terms. *PloS One* 6, e21800. doi: 10.1371/journal.pone.0021800

Taneri, P. E., Gómez-Ochoa, S. A., Llanaj, E., Raguindin, P. F., Rojas, L. Z., Roa-Díaz, Z. M., et al. (2020). Anemia and iron metabolism in COVID-19: a systematic review and meta-analysis. *Eur. J. Epidemiol.* 35, 763–773. doi: 10.1007/s10654-020-00678-5

Thipubon, P., Uthaipibull, C., Kamchonwongpaisan, S., Tipsuwan, W., and Srichairatanakool, S. (2015). Inhibitory effect of novel iron chelator, 1-(N-acetyl-6-aminohexyl)-3-hydroxy-2-methylpyridin-4-one (CM1) and green tea extract on growth of *Plasmodium falciparum*. *Malaria J.* 14, 382. doi: 10.1186/s12936-015-0910-1

Thomson-Luque, R., Votborg-Novél, L., Ndovie, W., Andrade, C. M., Niangaly, M., Attipa, C., et al. (2021). Plasmodium falciparum transcription in different clinical presentations of malaria associates with circulation time of infected erythrocytes. *Nat. Commun.* 12, 4711. doi: 10.1038/s41467-021-25062-z

Trager, W., and Jensen, J. B. (1976). Human malaria parasites in continuous culture. *Science.* 193, 673–675. doi: 10.1126/science.781840

van Esveld, S. L., Meerstein-Kessel, L., Boshoven, C., Baaij, J. F., Barylyuk, K., Coolen, J. P. M., et al. (2021). A prioritized and validated resource of mitochondrial proteins in *Plasmodium* identifies unique biology. *mSphere.* 6, e0061421. doi: 10.1128/mSphere.00614-21

Varadi, M., Anyango, S., Deshpande, M., Nair, S., Natassia, C., Yordanova, G., et al. (2022). AlphaFold Protein Structure Database: massively expanding the structural coverage of protein-sequence space with high-accuracy models. *Nucleic Acids Res.* 50, D439–DD44. doi: 10.1093/nar/gkab1061

Waller, K. L., Muhle, R. A., Ursos, L. M., Horrocks, P., Verdier-Pinard, D., Sidhu, A. B., et al. (2003). Chloroquine resistance modulated in *vitro* by expression levels of the Plasmodium falciparum chloroquine resistance transporter. *J. Biol. Chem.* 278, 33593–33601. doi: 10.1074/jbc.M302215200

Ward, D. M., and Kaplan, J. (2012). Ferroportin-mediated iron transport: Expression and regulation. *Biochim. Biophys. Acta (BBA) - Mol. Cell Res.* 1823, 1426–1433. doi: 10.1016/j.bbamcr.2012.03.004

Wichers, J. S., Mesén-Ramírez, P., Fuchs, G., Yu-Strzelczyk, J., Stäcker, J., von Thien, H., et al. (2022). PMRT1, a *Plasmodium*-specific parasite plasma membrane transporter, is essential for asexual and sexual blood stage development. *mBio.* 13, e00623–e00622. doi: 10.1128/mbio.00623-22

Wichers, J. S., Scholz, J. A. M., Strauss, J., Witt, S., Lill, A., Ehnold, L. I., et al. (2019). Dissecting the gene expression, localization, membrane topology, and function of the Plasmodium falciparum STEVOR protein family. *mBio* 10 (4), e01500-19. doi: 10.1128/mBio.01500-19

Wichers, J. S., van Gelder, C., Fuchs, G., Ruge, J. M., Pietsch, E., Ferreira, J. L., et al. (2021). Characterization of Apicomplexan Amino Acid Transporters (ApiATs) in the malaria parasite *Plasmodium falciparum*. *mSphere* 6, e00743–e00721. doi: 10.1128/mSphere.00743-21

Wunderlich, J. (2022). Updated list of transport proteins in Plasmodium falciparum. *Front. Cell Infect. Microbiol.* 12, 926541. doi: 10.3389/fcimb.2022.926541

Wunderlich, J., Kotov, V., Votborg-Novél, L., Ntalla, C., Geffken, M., Peine, S., et al. (2024). Iron transport pathways in the human malaria parasite *Plasmodium falciparum* revealed by RNA-sequencing. *bioRxiv*. doi: 10.1101/2024.04.18.590068

Wunderlich, J., Rohrbach, P., and Dalton, J. P. (2012). The malaria digestive vacuole. *Front. Biosci. (Schol Ed).* 4, 1424–1448. doi: 10.2741/s344

Zhang, L., Hendrickson, R. C., Meikle, V., Lefkowitz, E. J., Ioerger, T. R., and Niederweis, M. (2020). Comprehensive analysis of iron utilization by *Mycobacterium tuberculosis*. *PloS Pathog.* 16, e1008337. doi: 10.1371/journal.ppat.1008337

Zhang, M., Wang, C., Otto, T. D., Oberstaller, J., Liao, X., Adapa, S. R., et al. (2018). Uncovering the essential genes of the human malaria parasite *Plasmodium falciparum* by saturation mutagenesis. *Science* 360, eaap7847. doi: 10.1126/science.aap7847

Zhang, D.-L., Wu, J., Shah, B. N., Greutélaers, K. C., Ghosh, M. C., Ollivierre, H., et al. (2018). Erythrocytic ferroportin reduces intracellular iron accumulation, hemolysis, and malaria risk. *Science.* 359, 1520–1523. doi: 10.1126/science.aal2022